Electronic Supplementary Information (ESI)

Phenolate Based Metallomacrocyclic Xanthate Complexes of Co^{II}/ Cu^{II} and Their Exclusive Deployment in [2:2] Binuclear *N, O*-Schiff Base Macrocycle Formation and *in vitro* Anticancer Studies†

Rahul Kadu,[a] Vinay K. Singh,*[a] Hetal Roy,[b] Pallepogu Raghavaiah[c] and Shaikh M. Mobin[d]

† Dedicated to Professor Pradeep Mathur on the occasion of his 60th Birthday
[a]Department of Chemistry, Faculty of Science, The M. S. University of Baroda, Vadodara- 390 002, India
[b]Department of Zoology, Faculty of Science, The M. S. University of Baroda, Vadodara-390 002, India
[c]National Single Crystal X-ray Diffraction Facility, School of Chemistry, University of Hyderabad, Hyderabad-500 046, India
[d]National Single Crystal X-ray Diffraction Facility, IIT Bombay, Powai, Mumbai 400 076, India

*Email: vinay.singh-chem@msu.ac.in

Contents

General Methods and Materials. The reagents such as 4,4'-diaminodiphenyl ether (99%), CS_2 (99%), 2-hydroxybenzaldehyde (98%) and 2-hydroxynaphthaldehyde (98%) were purchased from National Chemicals, Merck and Chemlabs, respectively. All other chemicals were obtained from commercial sources and were used without further purification. All the reactions and manipulations were performed under an inert atmosphere.

Analytical Methods. Elemental analyses were performed on a Perkin-Elmer Series II CHNS/O Analyser 2400. Mass spectra were obtained on Thermo Scientific DSQ-II, Water's QTOF and AB SCIEX 3200 Q TRAP LC/MS/MS system. IR (KBr pellets) spectra were recorded in the

4000-400 cm^{-1} range using a Perkin-Elmer FTIR Spectrometer. The NMR spectra were obtained on a Bruker 400 MHz spectrometer in DMSO-d6 unless otherwise noted. Single crystal X-ray analysis was carried out on Oxford diffraction X-Calibur and Agilent's Gemini diffractometer equipped with Eos CCD detector. UV–visible spectra were recorded on a Perkin Elmer Lambda 35 UV–vis spectrophotometer. TGA/DTA plots were obtained using SII TG/DTA 6300 in flowing N_2 with a heating rate of 10 °C min^{-1}. GC analysis was carried out on CLARUS500, PE AutoSystem type GC equipped with FID detector. Powder X-ray diffraction studies were performed on a 'X Calibur, Eos, Gemini' X-ray diffractometer using Cu source, CrysAlisPro data reduction: Agilent Technologies Version 1.171.36.28 program(s) used to process the data and the 'POWDERX' program for indexing the powder XRD data.

Synthesis

Ligand precursors L^1 and L^2. To a solution of 2-hydroxybenzaldehyde (3 mmol, 366.36 mg) or 2-hydroxynaphthaldehyde (3 mmol, 516.54 mg) in 10 mL of toluene containing 2-3 drops of glacial acetic acid were added 4, 4'-diaminodiphenyl ether (1 mmol, 200 mg) with rigorous stirring. The reaction mixture was refluxed for 2 hrs using Dean-Stark apparatus. This reaction is outlined in Scheme S1. The reaction mixture was cooled at room temperature and solvent was evaporated under vacuum, washed with chilled absolute ethanol followed by diethyl ether to yield the products L^1 and L^2. These compounds were dried under vacuum and samples were taken for analysis.

4,4'-bis(*2*-hydroxybenzylideneamino)diphenyl ether (L^1). Yield: *ca* 404 mg, 99%, Mp: 213 °C. Anal. Calcd for [$C_{26}H_{20}N_2O_3$]: C, 76.45; H, 4.94; N, 6.86. Found: C, 76.40; H, 4.95; N, 6.89. Mass (MS ES+): 413.1730 (M+2Li), (42%); 414.1868 (M+2 Li+H), (10%). IR (KBr pellet, cm^{-1}): 3426m br ν(OH), 1618s ν(C=N). ^{1}H NMR (400 MHz, $CDCl_3$): (δ from TMS) 6.970(td, 2*H-Ph*), 7.05(dd, 2*H-Ph*), 7.115(dt, 4*H-Ph*), 7.34(dt, 4*H-Ph*), 7.41(m, 4*H-Ph*), 8.659(s, 2*H*-N=C*H*), 13.277(s, 2*H-OH*). ^{13}C NMR (400 MHz, $CDCl_3$): (δ from TMS) 117.29, 119.16, 119.70, 122.60, 132.25, 133.29, 156.17 (*all corresponds to Ph*), 161.19, 161.83(–N=*C*H). DEPT 135 (400 MHz, $CDCl_3$): (δ from TMS) 117.28, 119.16, 119.70, 122.61, 132.25, 133.20 (*all CH of Ph*), 161.84(–N=*C*H).

4,4'-bis(*2*-hydroxynaphthylmethylideneamino)diphenyl ether (L^2). 475 mg, 93% , Mp: 164 °C. Anal. Calcd for [$C_{34}H_{24}N_2O_3$]: C, 80.30; H, 4.76; N, 5.51. Found: C, 80.38; H, 4.72; N, 5.45. Mass (MS ES+): 510.52 (M+H); (30%). IR (KBr pellet, cm^{-1}): 3437s br ν(OH), 1619s ν(C=N). ^{1}H NMR (400 MHz, $CDCl_3$): (δ from TMS) 7.159(m, 6*H-Ph*), 7.38(m, 6*H-Ph*), 7.55(td, 2*H-Ph*), 7.754(d, 2*H-Ph*), 7.84(d, 2*H-Ph*), 8.15(d, 2*H-Ph*), 9.39(s, 2*H*-N=C*H*), 15.529(s, 2*H-OH*). ^{13}C NMR (400 MHz, $CDCl_3$): (δ from TMS) 108.97, 118.94, 119.93, 121.72, 121.97, 123.57, 127.43, 128.07, 129.42, 133.10, 136.31, 141.59, 155.05, 155.82 (*all corresponds to Ph*), 168.69; (–N=*C*H).

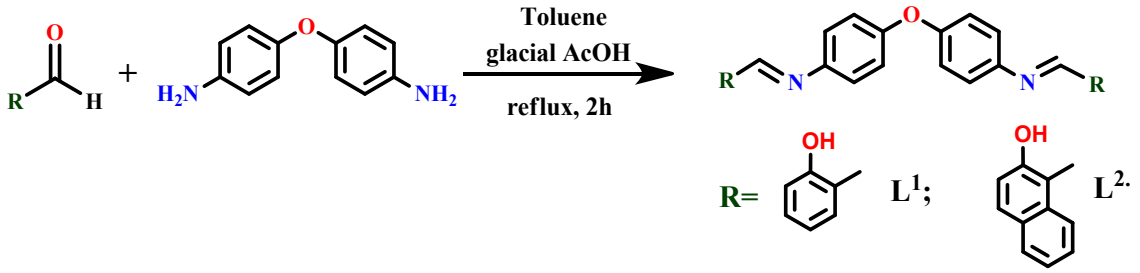

Scheme S1: General scheme for the synthesis of diimines L^1 and L^2.

Spectral Data

Characterization of L^1, L^2, K_2xan^1 and K_2xan^2. The broad peak appeared in the region of 3426-3437 cm^{-1} and the sharp peak in the region 1618-1619 cm^{-1} for L^1-L^2 are attributable to the ν(OH) and ν(N=C) vibrations respectively which is characteristic of Schiff bases and suggest the

formation of desired structures. The IR bands appeared are in accordance to the literature reports of similar compounds.[1] Disappearance of the IR absorption peak in the range of 3426-3437 cm^{-1} together with appearance of new bands in 1456-1493 cm^{-1} and 1084-1109 cm^{-1} region suggests the deprotonation of phenolic –OH and formation of $–OCSS_2$ moiety.

Schiff base precursors **L^1, L^2** and xanthate ligands **K_2xan^1**, **K_2xan^2** were characterized by ^1H and ^{13}C NMR. The signals appeared at 8.659 and 9.39 ppm in ^1H NMR spectra as well as signals appeared at 161.83 and 168.69 in ^{13}C NMR spectra for the precursors **L^1** and **L^2** respectively are due to –N=CH moiety which are the characteristic signals for the Schiff base compounds. Phenolic –OH have been appeared as a broad singlet at 13.277 and 15.529 ppm for **L^1** and **L^2** respectively. The remaining signals observed in the NMR spectra in the range of 6.57-8.15 ppm could be assigned to the aromatic hydrogen atoms which are generally obtained as multiplets, as a result of coupling of aromatic protons and 108-162 ppm to aromatic carbon atoms of Schiff base precursors. ^1H spectra of xanthate ligands **K_2xan^1** and **K_2xan^2** clearly showed the disappearance of signal for phenolic –OH which is previously present in **L^1** and **L^2** precursors. Generally, the most characteristic downfield signals appeared at 190.86 ppm and 190.24 ppm in the ^{13}C NMR spectra of xanthate ligands **K_2xan^1** and **K_2xan^2**, respectively evidently confirms the formation of xanthate moiety from phenolic –OH. Due to the incorporation of xanthate moiety in the molecule leads to the shifting of electron density from aromatic ring to xanthate moiety which results into the downfield signal (0.5-1.0 ppm) for –N=CH moiety compared to respective Schiff base precursor.

Mass spectral study. Notably, similar reactivity is depicted by the similar fragmentation pattern observed for a set of compounds i.e. for compounds bearing similar functionalities in the molecular framework. The binuclear macrocyclic complexes **2**, **6-7** were characterized by prominent molecular ion peak as shown in the mass spectra, summarized in Figure S1-S3.

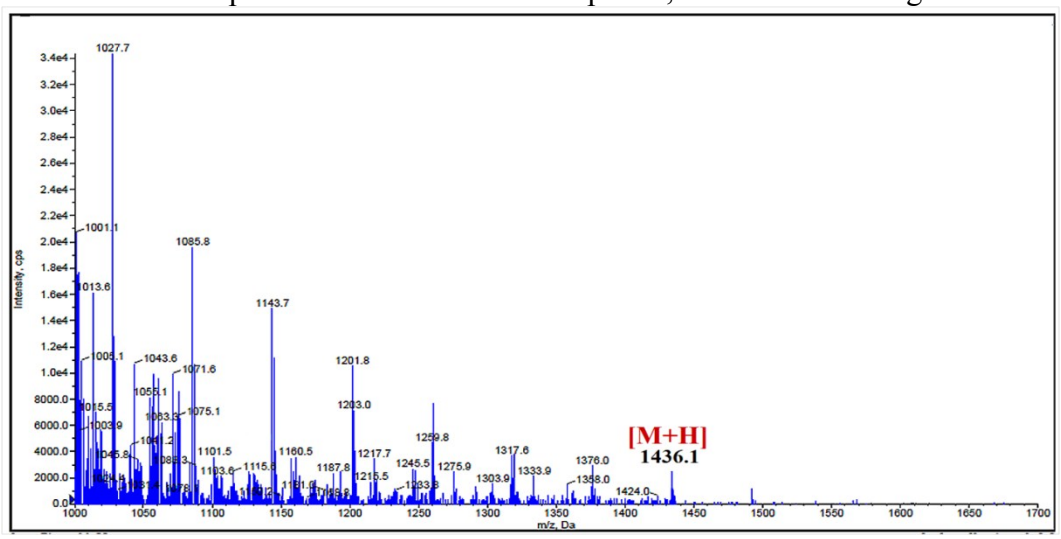

Figure S1. ES-MS of binuclear metallamacrocyclic Co^{II} xanthate complex **2**.

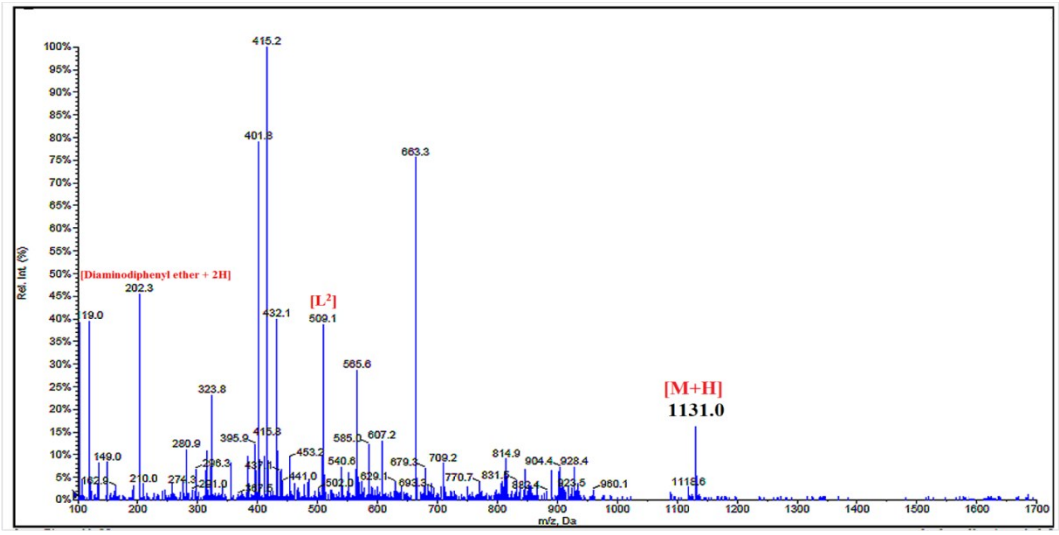

Figure S2. ES-MS of binuclear metallamacrocyclic Co^{II} *N, O*-Schiff base complex **6.**

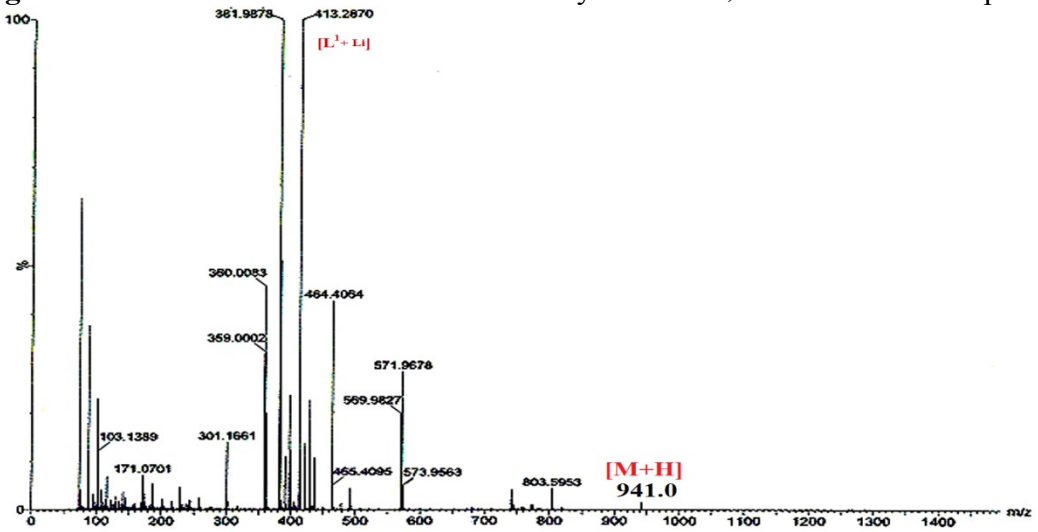

Figure S3. MALDI-TOF MS of binuclear metallamacrocyclic Cu^{II} *N, O*-Schiff base complex **7**.

The stacked IR spectra of $\mathbf{K_2xan^1}$, its binuclear xanthate complex **1** and corresponding binuclear *N,O*-Schiff base complex **5** as well as $\mathbf{K_2xan^1}$, its binuclear xanthate complex **3** and corresponding binuclear *N,O*-Schiff base complex **7** are given in Figure S4-S5, which clearly reveal the structural variations.

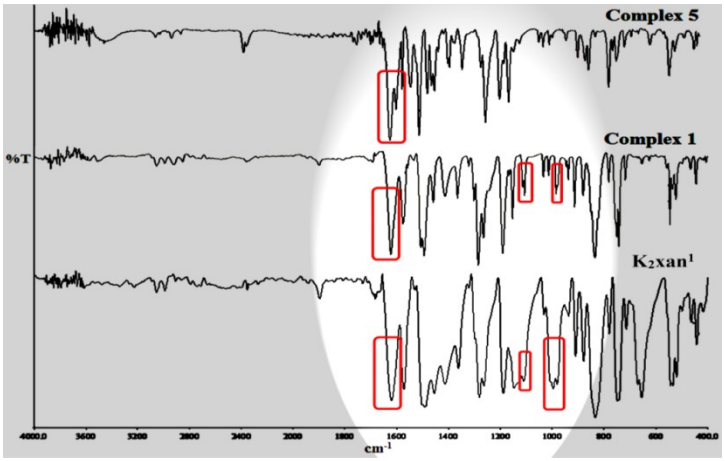

Figure S4: Representative IR spectra confirming the structural variation in $\mathbf{K_2xan^1}$, **1** and **5**.

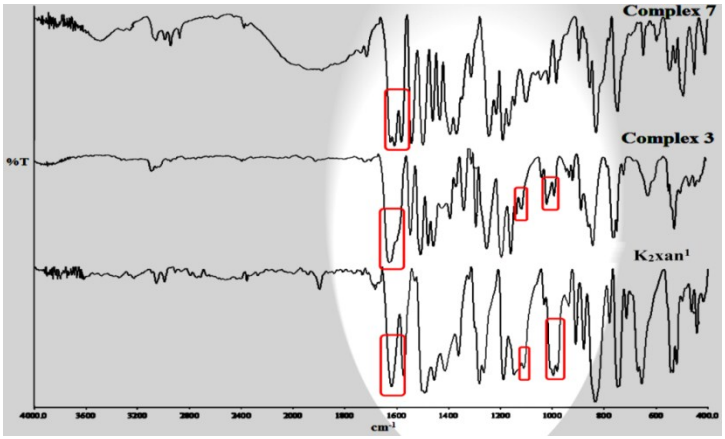

Figure S5: Representative IR spectra confirming the structural variation in **K_2xan^1**, **3** and **7**.

NMR spectral data

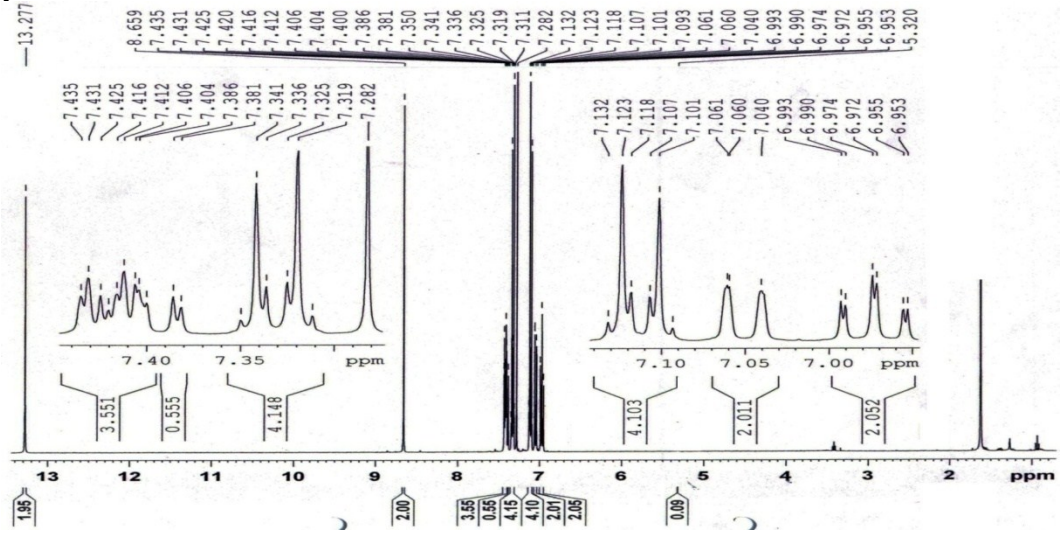

Figure S6. ^{1}H NMR spectrum for **L^1**

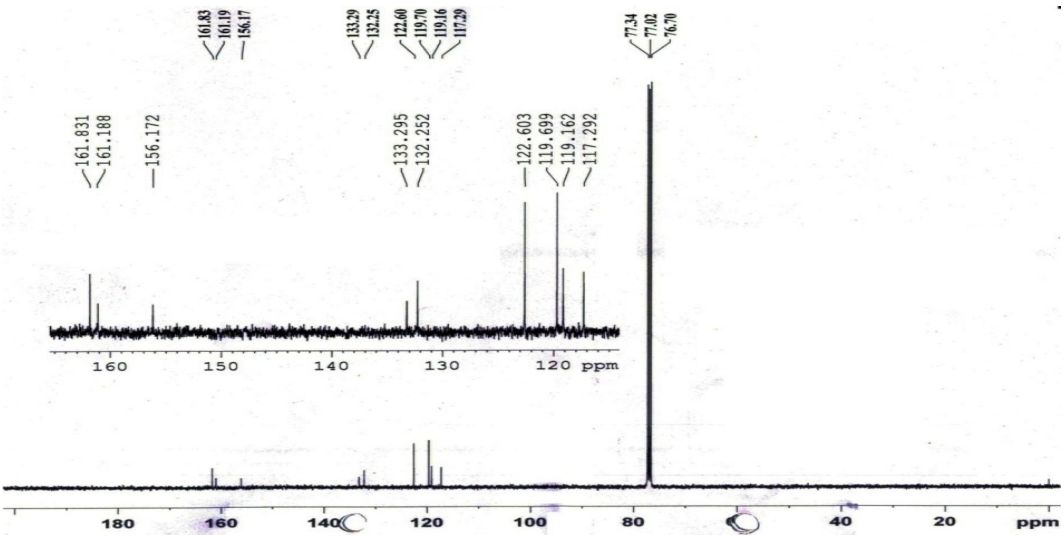

Figure S7.^{13}C NMR spectrum for **L^1**

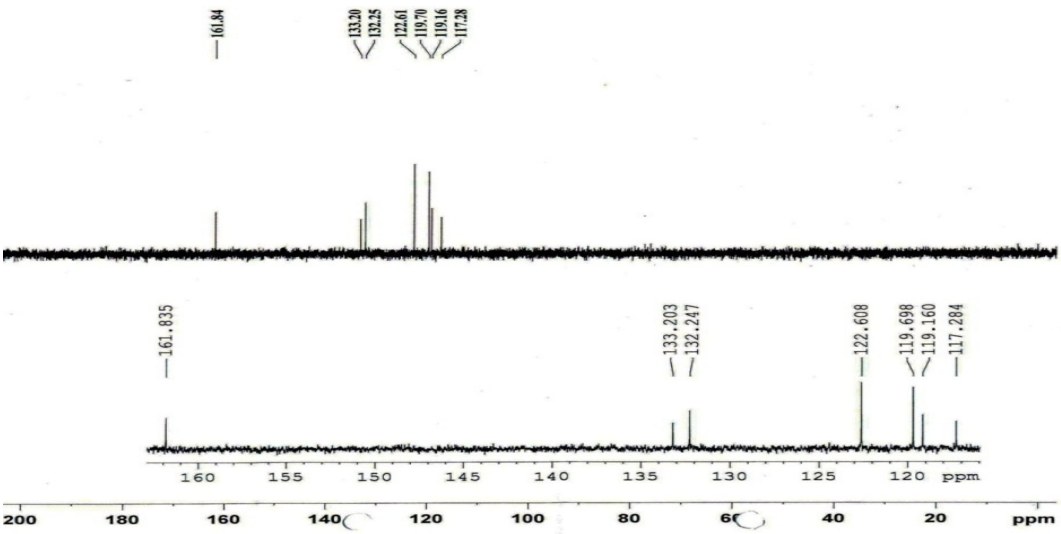

Figure S8. DEPT-135 NMR spectrum for **L[1]**

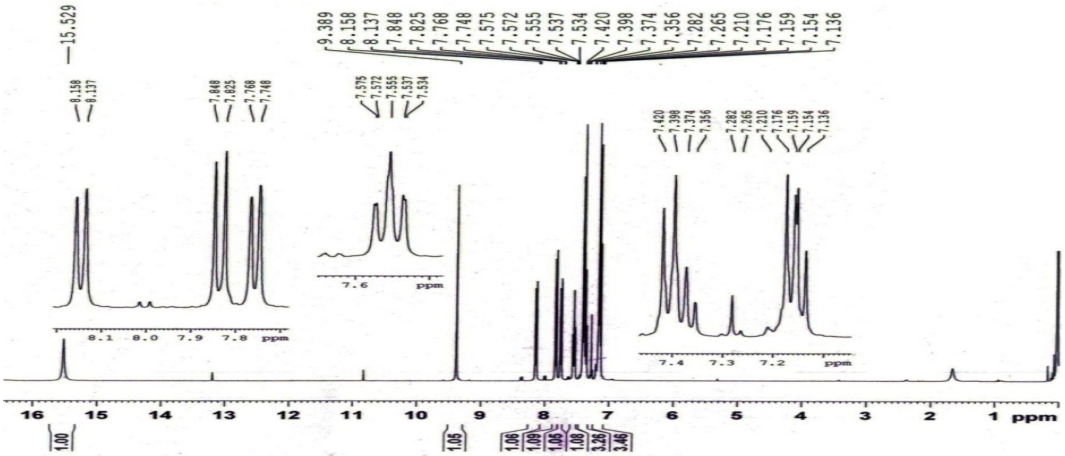

Figure S9. [1]H NMR spectrum for **L[2]**

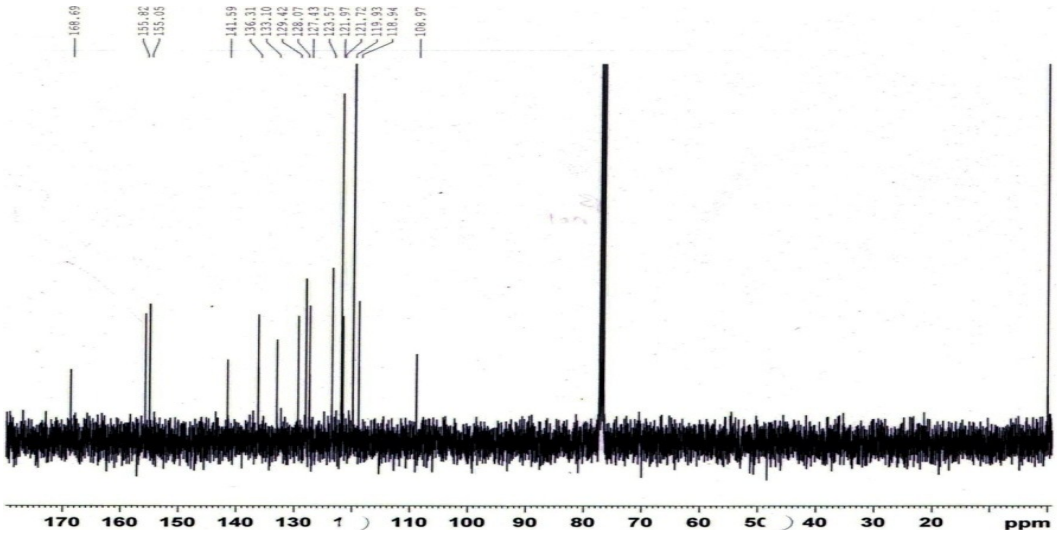

Figure S10. [13]C NMR spectrum for **L[2]**

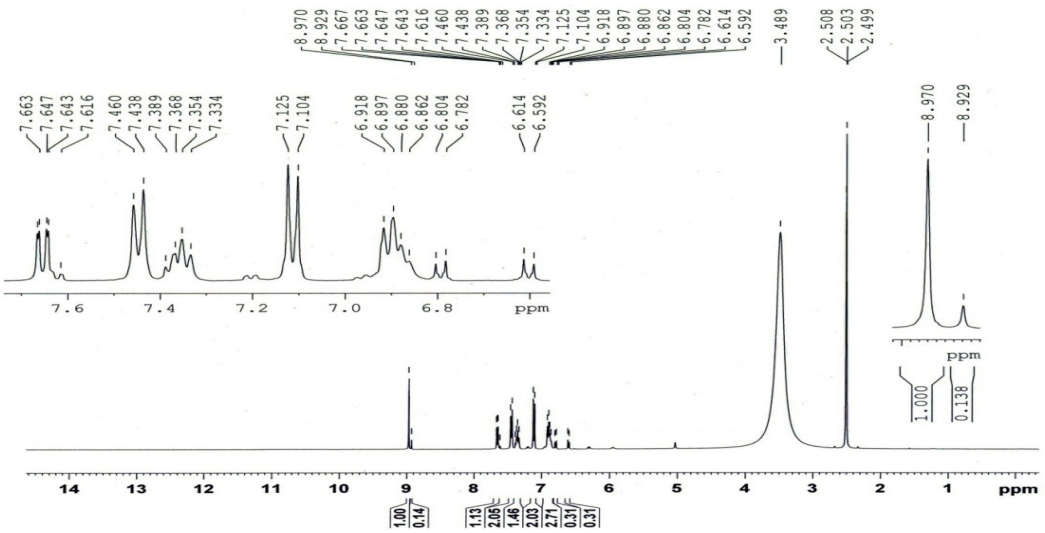

Figure S11. ^{1}H NMR spectrum for **K_2xan^1**

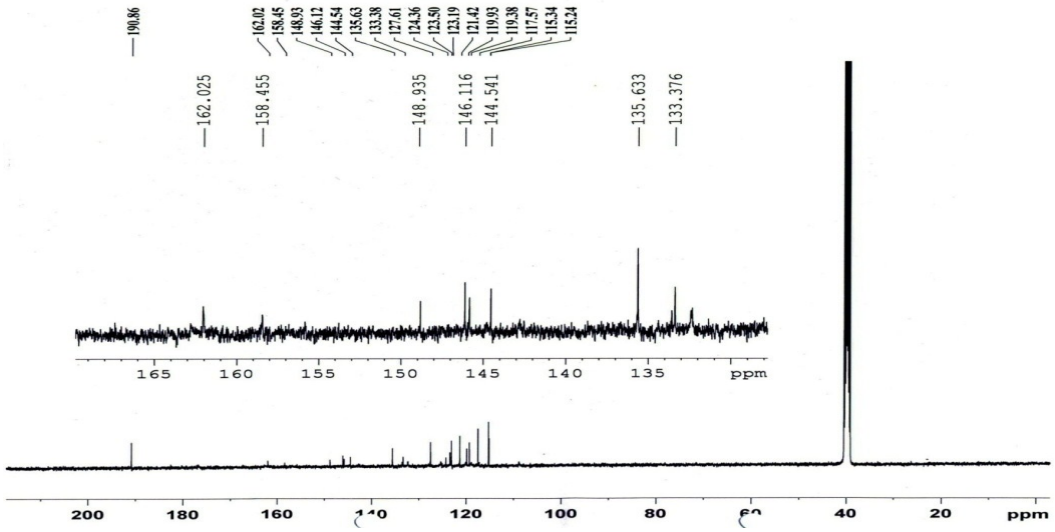

Figure S12. ^{13}C NMR spectrum for **K_2xan^1**

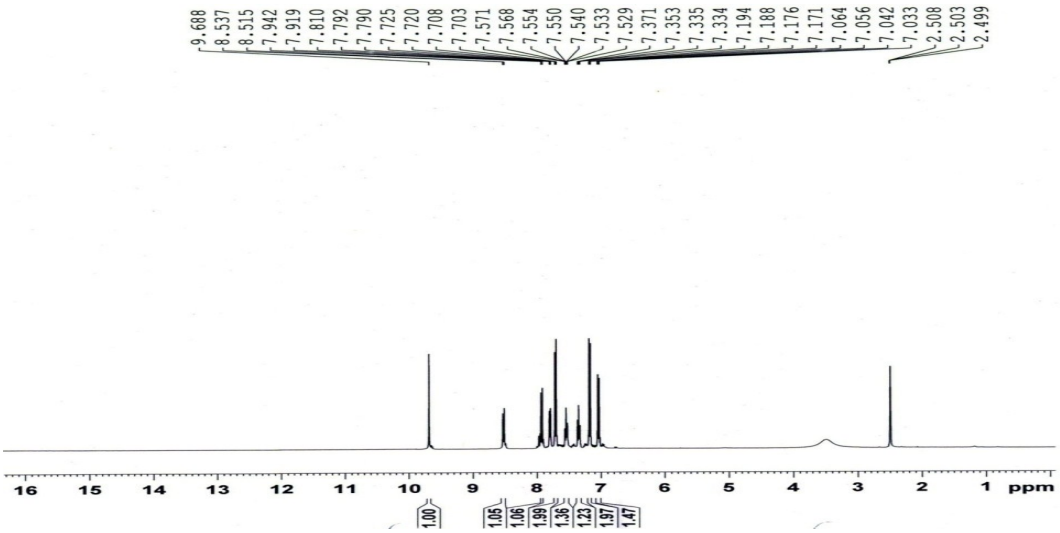

Figure S13. ^{1}H NMR spectrum for **K_2xan^2**

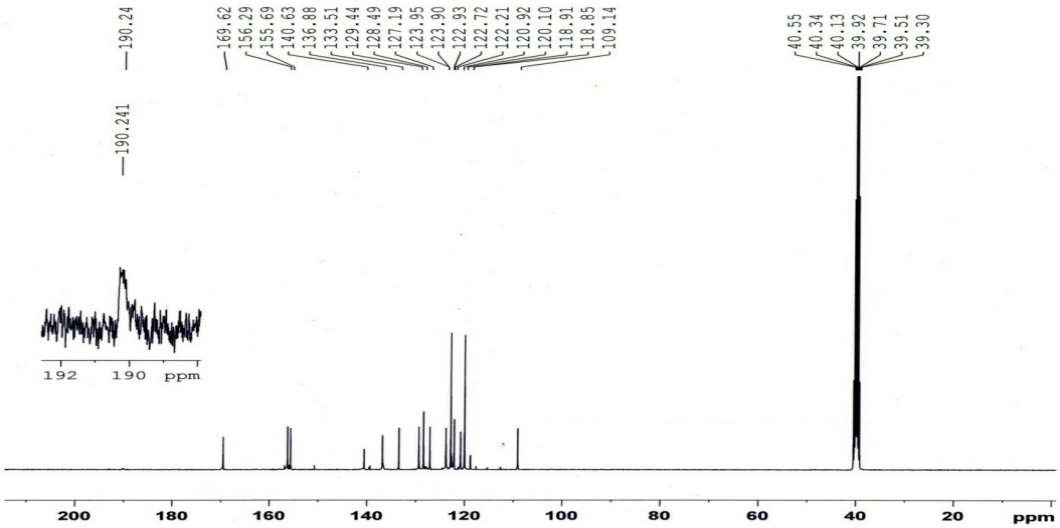

Figure S14. ^{13}C NMR spectrum for **K_2xan^2**

Powder XRD. The inadequate stability of the freshly synthesized xanthate ligands and their metal complexes in solvents, especially chlorinated solvents limited the crystallization attempts. Hence, the powder X-ray diffraction study performed on representative compounds (**K_2xan^1**, **1, 3, 5** and **7**) and it suggests the microcrystalline nature of these samples. Further it helped us to understand structural characteristics like crystal lattice, lattice parameters. Notably, the results of the XRD analysis for xanthate ligand **K_2xan^1** and its Co^{II}/Cu^{II} complexes **1** and **3** as well as their corresponding Schiff base complexes **5** and **7** do not match well as they have different crystal packing. (Figure S15 and S16) In spite of their structural differences, there persists some obvious similarity in the patterns in these compounds because of the presence of the common molecular framework which remains intact during the course of the preparation.

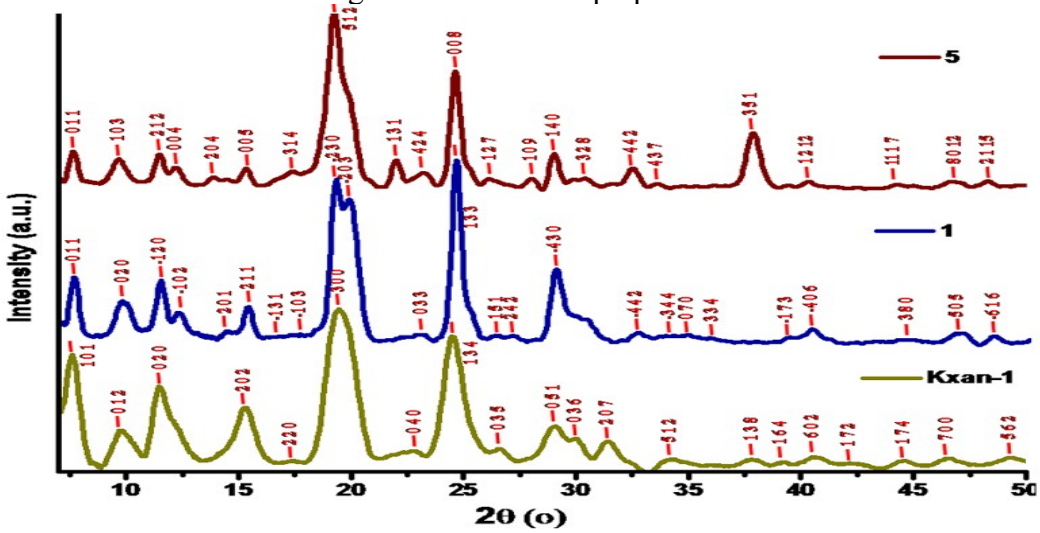

Figure S15. Powder X-ray diffraction pattern for a set of compounds **K_2xan ^{1}, 1** and **5**

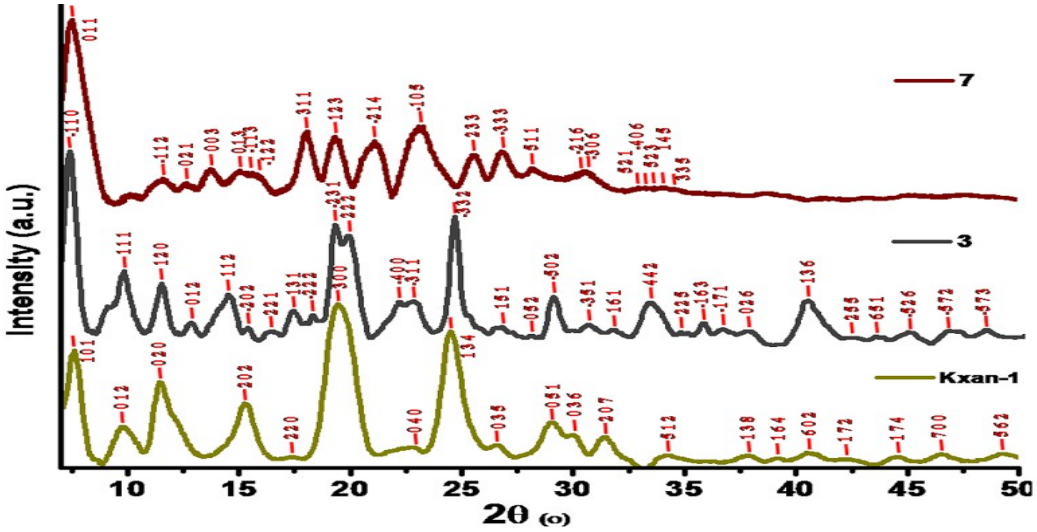

Figure S16. Powder X-ray diffraction pattern for a set of compounds **K_2xan [1], 3** and **7.** The powder XRD data for these samples have been successfully indexed and refined by least square refinement with the help of commonly used[2] program[3] 'POWDERX' and the details of the indexed peak are given in Table S1.

Table S1. Power X-ray diffraction data for **K_2xan[1]**, **1, 3, 5** and **7**.

Powder pattern line	h	k	l	2θ			d spacing		Intensity
				Exp.	Calc.	Diff	Exp.	Calc.	
(a) Kxan-1: *Orthorhombic (P)*: a = 13.66 Å, b = 15.5 Å, c = 21.9 Å; $\alpha = \beta = \gamma = 90^o$.									
1	1	0	1	7.619	7.627	-0.009	11.60344	11.59019	25.63
2	0	1	2	9.838	9.89	-0.051	8.98996	8.9434	9.02
3	0	2	0	11.483	11.417	0.066	7.70575	7.75	18.69
4	2	0	2	15.263	15.289	-0.026	5.805	5.79509	14.07
5	2	2	0	17.32	17.305	0.014	5.11985	5.12409	2.36
6	3	0	0	19.453	19.495	-0.042	4.563	4.55333	35.61
7	0	4	0	22.908	22.95	-0.042	3.88204	3.875	4.52
8	1	3	4	24.522	24.57	-0.048	3.63006	3.62308	29.67
9	0	3	5	26.629	26.681	-0.052	3.34736	3.34101	4.98
10	0	5	1	29.081	29.092	-0.01	3.07046	3.0694	9.95
11	0	3	6	30.004	29.973	0.031	2.97812	2.98113	7.23
12	2	0	7	31.448	31.45	-0.002	2.84453	2.84436	6.63
13	5	1	2	34.23	34.32	-0.09	2.6195	2.61281	2.72
14	1	3	8	37.79	37.767	0.023	2.38051	2.38188	2.68
15	1	6	4	39.134	39.115	0.019	2.30179	2.30288	2.1
16	6	0	2	40.502	40.467	0.035	2.22716	2.229	3.26
17	1	7	2	42.134	42.157	-0.023	2.1446	2.14347	1.93
18	1	7	4	44.641	44.637	0.004	2.02979	2.02996	2.42
19	7	0	0	46.537	46.537	0	1.95142	1.95143	2.95
20	5	6	2	49.268	49.251	0.017	1.84946	1.85006	3.06
21	4	2	10	50.919	50.914	0.005	1.7933	1.79345	1.94
(b) 1: *Monoclinic (P)*: a = 14.5 Å, b = 18.03 Å, c = 15.35 Å; $\alpha = \gamma = 90^o$ and $\beta = 99.1^o$.									
1	0	1	1	7.683	7.62	0.063	11.49785	11.59306	1.25
2	0	2	0	9.82	9.811	0.009	9.00002	9.00809	0.86
3	-1	2	0	11.522	11.599	-0.077	7.67391	7.62287	1.18
4	-1	0	2	12.321	12.32	0.002	7.17773	7.17873	0.67
5	2	0	1	14.492	14.495	-0.003	6.10719	6.10592	0.36
6	2	1	1	15.398	15.31	0.088	5.74981	5.78283	0.75
7	-1	3	1	16.704	16.693	0.011	5.30297	5.30644	0.28
8	-1	0	3	17.692	17.667	0.025	5.0091	5.01614	0.31

9	-2	3	0	19.275	19.282	-0.007	4.60117	4.59942	2.83
10	-2	0	3	19.847	19.841	0.006	4.46979	4.47121	2.51
11	0	3	3	22.998	22.996	0.002	3.8641	3.86435	0.3
12	1	3	3	24.588	24.559	0.029	3.61765	3.6219	3.15
13	1	5	1	26.343	26.377	-0.033	3.38043	3.37623	0.29
14	2	4	2	27.079	27.041	0.038	3.29029	3.29484	0.29
15	-4	3	0	29.006	29.035	-0.028	3.07587	3.07292	1.37
16	-4	4	2	32.63	32.659	-0.029	2.74208	2.73972	0.33
17	-3	4	4	34.158	34.175	-0.017	2.62283	2.6216	0.29
18	0	7	0	34.816	34.83	-0.014	2.57472	2.57374	0.3
19	3	3	4	35.797	35.773	0.024	2.50643	2.50807	0.25
20	-1	7	3	39.317	39.314	0.003	2.28973	2.28991	0.26
21	-4	0	6	40.303	40.31	-0.007	2.23597	2.23561	0.39
22	3	8	0	44.459	44.453	0.005	2.03614	2.03638	0.22
23	5	0	5	46.979	46.969	0.01	1.9326	1.933	0.33
24	-6	1	6	48.394	48.415	-0.021	1.87934	1.87858	0.28
25	-7	1	5	49.951	49.944	0.007	1.82436	1.82459	0.21
26	-8	0	1	50.389	50.386	0.003	1.80953	1.80962	0.22

(c) 3: *Monoclinic (P)*: $\boldsymbol{a}$ = 16.2 Å, $\boldsymbol{b}$ = 17.6 Å, $\boldsymbol{c}$ = 15.0 Å; $\boldsymbol{\alpha} = \boldsymbol{\gamma}$ = 90º and $\boldsymbol{\beta}$ = 96.15º.

1	-1	1	0	7.418	7.44	-0.022	11.90844	11.87299	2.87
2	1	1	1	9.816	9.877	-0.061	9.00346	8.94781	1.15
3	1	2	0	11.517	11.458	0.059	7.67723	7.71664	0.97
4	0	1	2	12.841	12.893	-0.052	6.88836	6.86074	0.41
5	1	1	2	14.5	14.514	-0.015	6.10404	6.09798	0.81
6	-2	0	2	15.355	15.304	0.052	5.76569	5.78502	0.34
7	2	2	1	16.476	16.491	-0.015	5.37596	5.371	0.28
8	1	3	1	17.397	17.354	0.043	5.09336	5.10601	0.58
9	-2	2	2	18.264	18.343	-0.079	4.85355	4.83291	0.52
10	-2	3	1	19.271	19.28	-0.009	4.60208	4.60006	1.82
11	2	2	2	19.856	19.829	0.027	4.46783	4.4739	1.66
12	-4	0	0	22.124	22.074	0.05	4.01464	4.0236	0.7
13	-3	3	1	22.776	22.769	0.007	3.90114	3.90234	0.72
14	-3	3	2	24.581	24.602	-0.021	3.61867	3.6156	1.94
15	1	5	1	26.725	26.736	-0.011	3.33303	3.3317	0.34
16	0	5	2	28.033	28.03	0.003	3.18038	3.18073	0.22
17	-5	0	2	29.005	28.992	0.014	3.076	3.0774	0.78
18	-3	5	1	30.578	30.607	-0.029	2.92123	2.91855	0.38
19	1	6	1	31.704	31.692	0.012	2.82005	2.82105	0.3
20	4	4	2	33.32	33.337	-0.017	2.68683	2.6855	0.7
21	2	2	5	34.68	34.701	-0.021	2.58453	2.583	0.27
22	-1	6	3	35.675	35.671	0.003	2.51473	2.51494	0.4
23	-1	7	1	36.539	36.571	-0.032	2.45719	2.45514	0.31
24	0	2	6	37.577	37.601	-0.024	2.39167	2.39019	0.28
25	1	3	6	40.35	40.346	0.004	2.23349	2.23369	0.72
26	2	5	5	42.142	42.136	0.006	2.14254	2.14284	0.19
27	6	5	1	43.357	43.328	0.029	2.08528	2.08662	0.21
28	-5	2	6	44.829	44.802	0.027	2.02017	2.02133	0.27
29	-5	7	2	46.64	46.632	0.007	1.94587	1.94617	0.29
30	-5	7	3	48.298	48.298	0	1.88287	1.88287	0.31
31	2	8	4	50.076	50.049	0.026	1.82011	1.821	0.22

(d) 5: *Orthorhombic (P)*: $\boldsymbol{a}$ = 26.4 Å, $\boldsymbol{b}$ = 12.4 Å, $\boldsymbol{c}$ = 28.9 Å; $\boldsymbol{\alpha} = \boldsymbol{\beta} = \boldsymbol{\gamma}$ = 90º.

1	0	1	1	7.669	7.758	-0.089	11.52802	11.39535	6.54
2	1	0	3	9.707	9.773	-0.067	9.11165	9.04967	5.3
3	2	1	2	11.503	11.548	-0.046	7.69266	7.66242	6.15
4	0	0	4	12.229	12.25	-0.021	7.23732	7.225	3.96
5	2	0	4	13.916	13.973	-0.057	6.3636	6.33774	2.35
6	0	0	5	15.351	15.329	0.022	5.77169	5.78	3.77
7	3	1	4	17.405	17.417	-0.012	5.09508	5.0916	3.31

8	5	1	2	19.266	19.275	-0.009	4.60686	4.60468	29.43
9	1	3	1	22.003	21.982	0.021	4.03965	4.04342	5.15
10	4	2	4	23.248	23.216	0.033	3.82592	3.83121	3.07
11	0	0	8	24.634	24.643	-0.008	3.6137	3.6125	19.66
12	1	2	7	26.144	26.15	-0.006	3.40841	3.40765	2.09
13	1	0	9	28.032	27.99	0.041	3.183	3.18762	2.11
14	1	4	0	29.024	29	0.024	3.07635	3.07884	6.17
15	3	2	8	30.381	30.384	-0.002	2.94198	2.94175	2.16
16	4	4	2	32.507	32.505	0.002	2.75424	2.75445	3.83
17	4	3	7	33.585	33.549	0.037	2.66828	2.67111	1.3
18	3	5	1	37.862	37.816	0.046	2.37616	2.37892	9.6
19	1	2	12	40.313	40.319	-0.006	2.23716	2.23684	1.62
20	11	1	7	44.245	44.259	-0.014	2.04703	2.04644	1.14
21	8	0	12	46.716	46.69	0.025	1.94437	1.94537	1.67
22	2	1	15	48.292	48.297	-0.005	1.88451	1.88432	1.7
23	13	2	6	50.971	50.976	-0.005	1.7916	1.79144	3.74
24	0	1	1	7.669	7.758	-0.089	11.52802	11.39535	6.54

(e) 7: *Monoclinic (P)*: $\boldsymbol{a}$ = 16.8 Å, $\boldsymbol{b}$ = 15.0 Å, $\boldsymbol{c}$ = 19.4 Å; $\boldsymbol{\alpha} = \boldsymbol{\gamma}$ = 90º and $\boldsymbol{\beta}$ = 96.15º**.**

1	0	1	1	7.517	7.466	0.051	11.7514	11.83181	4.02
2	-1	1	2	11.623	11.69	-0.067	7.60747	7.56428	0.94
3	0	2	1	12.686	12.663	0.023	6.97228	6.9848	0.86
4	0	0	3	13.747	13.773	-0.025	6.43629	6.42452	1.12
5	0	1	3	15.077	14.991	0.085	5.8717	5.90494	1.1
6	-1	1	3	15.405	15.404	1E-3	5.74709	5.74761	1.06
7	-1	2	2	15.638	15.547	0.092	5.66202	5.69519	1.05
8	3	1	1	18.089	18.045	0.044	4.90001	4.91183	1.85
9	1	2	3	19.365	19.354	0.01	4.58006	4.58248	1.76
10	-2	1	4	21.117	21.111	0.006	4.20384	4.20503	1.67
11	-1	0	5	23.119	23.099	0.02	3.84401	3.8473	1.96
12	2	3	3	25.565	25.588	-0.023	3.48158	3.4785	1.4
13	-3	3	3	26.818	26.813	0.005	3.32162	3.32223	1.46
14	5	1	1	28.248	28.228	0.019	3.15672	3.15886	1.14
15	-2	1	6	29.307	29.29	0.017	3.04494	3.04672	0.97
16	-3	0	6	30.638	30.584	0.053	2.9157	2.92065	1.09
17	5	3	1	32.986	32.985	0	2.71333	2.71336	0.76
18	-4	0	6	33.284	33.301	-0.016	2.68967	2.68838	0.77
19	5	2	3	33.715	33.72	-0.005	2.65629	2.6559	0.76
20	1	4	5	34.163	34.167	-0.004	2.62243	2.62215	0.78
21	3	3	5	34.618	34.675	-0.057	2.58902	2.58492	0.75

In case of binuclear Schiff base complex **5** and **7**, deviation between the experimental powder XRD pattern and simulated powder XRD pattern obtained from single crystal X-ray diffraction study shows that the bulk properties of these materials are different from the single crystals obtained upon very slow evaporation of solvent. Notably the powder XRD data could be indexed in the similar lattice system as that of single crystals for **5** and **7** however the differences in the cell parameters probably arise due to the involvement of solvent molecules stabilizing the crystal structure.

X-ray Crystallography

Table S2 Crystal data and structure refinement for compounds 5-8.

Compound	**5**	**6**	**7. *DMSO***	**7. *$2CH_2Cl_2$***	**8. *$CHCl_3.8H_2O$***
CCDC Number	986524	986523	986525	986526	1426720
Formula	$C_{52}H_{36}Co_2N_4O_6$	$C_{68}H_{44}Co_2N_4O_6$	$C_{54}H_{42}Cu_2N_4O_7S$	$C_{54}H_{40}Cl_4Cu_2N_4O_6$	$C_{137}H_{104}Cl_3Cu_4N_8O_{20}$
Formula weight(amu)	930.71	1130.93	1018.06	1109.80	2526.66
T(K)	293(2)	298.15	295.0	150(2)	298.15
Crystal System	orthorhombic	monoclinic	orthorhombic	monoclinic	monoclinic
Space group	Pbca	$P2_1/c$	Pbca	C2/c	$P2_1/c$
a(Å)	26.3438(6)	11.840(3)	26.2828(4)	16.5132(3)	19.0398(9)
b(Å)	12.3067(3)	12.679(3)	12.25878(17)	14.6766(2)	21.6349(7)
c(Å)	28.9628(7)	37.680(8)	28.8218(4)	19.2170(3)	31.0856(15)
α(°)	90.00	90.00	90.00	90.00	90.00
β(°)	90.00	95.358(4)	90.00	96.1890(10)	100.470(5)
γ(°)	90.00	90.00	90.00	90.00	90.00
Cell volume ($Å^3$)	9389.9(4)	5632(2)	9286.2(2)	4630.24(13)	12591.7(9)
Z	8	4	8	4	4
Completeness to theta (%)	(θ = 72.16) 100	(θ = 26.08) 99.7	(θ = 27.36) 96.27	(θ = 25.00) 99.8	(θ = 26.08) 99.7
$\rho_{calc}g/cm^3$	1.317	1.334	1.456	1.592	1.333
μ/mm^{-1}	5.965	0.647	1.020	1.209	0.800
F(000)	3824.0	2328.0	4192.0	2264.0	5172.0
Radiation	CuKα (λ = 1.54184)	MoKα (λ = 0.71073)	Mo Kα (λ = 0.71073)	MoKα (λ = 0.71073)	MoKα (λ = 0.71073)
2θ range for data collection/°	9.84 to 144.32	3.4 to 52.16	6.38 to 54.72	6.88 to 50	6.58 to 65.68
Index ranges	$-31 \le h \le 31$, $-14 \le k \le 7$, $-35 \le l \le 35$	$-14 \le h \le 14$, $-15 \le k \le 15$, $-46 \le l \le 46$	$0 \le h \le 33$, $0 \le k \le 15$, $0 \le l \le 36$	$-19 \le h \le 19$, $-16 \le k \le 17$, $-22 \le l \le 22$	$-28 \le h \le 26$, $-29 \le k \le 31$, $-46 \le l \le 44$
Reflections collected	23584	58626	10072	17040	160890
Independent reflections	8695 [R_{int} = 0.0385, R_{sigma} = 0.0507]	11149 [R_{int} = 0.0774, R_{sigma} = 0.0678]	10072 [R_{int} = 0.0000, R_{sigma} = 0.0254]	4085 [R_{int} = 0.0177, R_{sigma} = 0.0151]	42728 [R_{int} = 0.1895, R_{sigma} = 0.5255]
Data/restraints/parameters	8695/0/577	11149/0/721	10072/0/632	4085/0/316	42728/2/793
Goodness-of-fit on F^2	1.113	0.861	1.002	1.070	0.740
Final R indices [$I>2\sigma(I)$]	R_1 = 0.0593, wR_2 = 0.1861	R_1 = 0.0581, wR_2 = 0.1333	R_1 = 0.0391, wR_2 = 0.1117	R_1 = 0.0247, wR_2 = 0.0693	R_1 = 0.1272, wR_2 = 0.3435
R indices (all data)	R_1 = 0.0959, wR_2 = 0.2087	R_1 = 0.1301, wR_2 = 0.1555	R_1 = 0.0547, wR_2 = 0.1200	R_1 = 0.0285, wR_2 = 0.0702	R_1 = 0.4173, wR_2 = 0.3977
Largest diff. peak/hole / e $Å^{-3}$	0.40/-0.28	0.44/-0.19	0.33/-0.62	0.42/-0.57	1.54/-0.55

Table S3 Selected structural parameters of **5-7** from single crystal X-ray study.

Selected Bonds	Bond lengths (Å)	Selected Bonds	Bond angles (°)
	5		
O_6—Co_1	1.901(3)	N_4—Co_1—O_6	94.61(15)
O_{29}—Co_1	1.890(4)	N_9—Co_1—O_{29}	95.24(15)
O_5—Co_2	1.884(3)	N_9—Co_1—O_6	141.76(18)
O_{15}—Co_2	1.908(4)	N_4—Co_1—O_{29}	140.78(19)
N_4—Co_1	1.954(4)	N_3—Co_2—O_{15}	91.71(16)
N_9—Co_1	1.988(4)	N_{16}—Co_2—O_5	93.44(16)
N_3—Co_2	1.972(4)	N_3—Co_2—O_5	148.85(17)
N_{16}—Co_2	1.986(4)	N_{16}—Co_2— O_{15}	146.15(19)
N_3—C_{40}	1.283(6)	N_3—C_{40}— C_{52}	126.9(5)
N_{16}—C_7	1.432(6)	N_{16}—C_7— C_{14}	120.0(4)
N_4—C_{19}	1.422(6)	N_4—C_8— C_{13}	127.2(4)
N_9—C_{36}	1.427(6)	N_9—C_{32}— C_{64}	127.8(5)
		C_{39}—O_{17}— C_{34}	115.6(4)
		C_{31}—O_{12}— C_{43}	117.7(4)
	6		
O_3—Co_1	1.893(2)	N_1—Co_1—O_4	94.27(13)
O_4—Co_1	1.897(3)	N_2—Co_1—O_3	93.62(11)
O_5—Co_2	1.888(3)	N_1—Co_1—O_3	125.32(12)
O_6—Co_2	1.894(3)	N_2—Co_1—O_4	121.76(13)
N_1—Co_1	1.981(3)	N_3—Co_2—O_5	93.87(13)
N_2—Co_1	1.972(3)	N_4—Co_2—O_6	93.62(14)
N_3—Co_2	1.980(3)	N_3—Co_2—O_6	122.19(14)
N_4—Co_2	1.981(3)	N_4—Co_2—O_5	119.57(13)
N_1—C_{25}	1.292(4)	N_3—C_{47}— C_{48}	127.7(4)
N_2—C_{36}	1.302(4)	N_4—C_{58}— C_{59}	126.6(4)
N_3—C_{47}	1.296(5)	N_2—C_{36}— C_{37}	127.9(3)
N_4—C_{58}	1.311(5)	N_1—C_{25}— C_{26}	129.2(4)
		C_4—O_1— C_7	116.4(3)
		C_{16}—O_2— C_{19}	118.0(3)
	7.DMSO		
O_1— Cu_1	1.8922(17)	O_1—Cu_1— N_{10}	143.99(9)
O_2—Cu_1	1.9012(16)	O_2—Cu_1— N_{11}	144.84(8)
N_{10}—Cu_1	1.9492(17)	O_1—Cu_1— N_{11}	94.98(7)
N_{11}—Cu_1	1.9757(18)	O_2—Cu_1— N_{10}	94.33(7)
O_3— Cu_2	1.9081(17)	O_3— Cu_2— N_4	91.68(7)
O_4—Cu_2	1.8876(16)	O_4— Cu_2— N_{21}	93.43(8)
N_4—Cu_2	1.9766(19)	O_3— Cu_2— N_{21}	148.32(8)
N_{21}—Cu_2	1.9822(19)	O_4— Cu_2— N_4	150.90(8)
N_4—C_7	1.292(3)	N_{10}—C_{15}— C_{27}	126.5(2)
N_{21}—C_{23}	1.297(3)	N_{11}—C_{37}— C_{44}	120.7(2)
N_{10}—C_{15}	1.304(3)	N_4—C_7— C_{54}	126.2(2)
N_{11}—C_{53}	1.288(3)	N_{21}—C_{23}— C_{29}	127.8(2)
		C_{28}—O_5— C_{30}	115.42(18)
		C_{20}—O_6— C_{42}	117.50(17)
	7.CH_2Cl_2		
O_1— Cu_1	1.893(13)	O_3—Cu_1— N_2	94.92(6)
O_3—Cu_1	1.888(12)	O_1—Cu_1— N_1	94.11(6)
N_2—Cu_1	1.976(14)	N_2—Cu_1— O_1	145.89(6)
N_1—Cu_1	1.957(14)	N_1—Cu_1— O_3	145.29(6)
N_2—C_{20}	1.298(2)	C_6— C_7— N_1	125.87(17)
		C_{19}— C_{20}— N_2	126.81(16)
		C_{11}— O_2—C_{24}	115.91(13)

Description of Crystal Packing Patterns. The aromatic moieties present in the molecular framework potentially provide a hydrophobic surface capable of participating in noncovalent interactions such as $\pi...\pi$, CH...π, CH...O, Cl...O and/ or O...S in compounds **5-7**. The details about non-covalent interactions like interatomic distances (Å), bond angles and α, β angles (°) are summarized in Table S2. The favorable α angles (angle between the line connecting Cg, H

atom and the normal to the phenyl ring plane) whereas the β angles (Figure S17) are large enough to facilitate CH... π interactions found in normal range, reflects strength of particular interactions.

Table S4. Significant intermolecular interactions [Interatomic distances (Å), and bond angles (°)] found in compounds **5-7**.

Interactions	D─H…A		D─H	H…A	D…A	<DHA	<α	<β
			5					
CH…π	**H24...π** (Cg: C22 C60 C53 C46 C63 C44) **10 atoms**		0.932	2.590	3.521	176.87	5.3	176.87
	H61...π(Cg: C49 C59 C57 C52 C33 C55) **10 atoms**		0.930	2.751	3.583	149.11	11.99	149.11
	H49...π(Cg: C35 C11 C13 C20 C54 C42) **10 atoms**		0.931	2.908	3.682	141.48	2.12	141.48
	H62...π(Cg: C11 C35 C42 C54 H49 C20 C13) **10 atoms**		0.930	2.850	3.529	130.80	7.62	130.80
CH…O	**H8...O5/O15**	H8...O5	0.931	2.471	3.278	145.20	…	…
	(Bifurcated)	H8...O15	0.931	2.491	3.321	148.66	…	…
	H21...O15		0.931	2.519	3.205	130.71	…	…
	H59...O6		0.929	2.586	3.378	143.48	…	…
			6					
CH…π	**H6...π** (Cg: C70 C69 C32 C27 C28 C29)		0.932	2.850	3.485	126.40	1.01	126.40
	H15...π(Cg: C46 C37 C38 C43 C44 C45)		0.929	2.779	3.663	159.22	13.45	159.22
	H21...π(Cg: N4 C59 C60)		0.931	2.960	3.478	116.62	0.70	116.62
	H34...π(Cg: C17 C18 C13 C14 C15 C16)		0.929	3.419	4.140	136.23	40.68	136.23
	H42...π(Cg: C56 C57 C48 C49 C54 C55)		0928	3.758	4.443	132.99	44.91	132.99
	H55...π(Cg: C66 C65 C60 C59 C68 C67)		0.931	2.928	3.806	157.80	13.12	157.80
	H61...π(Cg: C56 C57 C48 C49 C54 C55)		0.931	3.190	3.826	126.42	5.44	126.42
π…π	**π...π** (Cg1: C7 C8 C9 C10 C11 C12, Cg2: C46 C37 C38 C43 C44 C45)		…	…	3.586	…	…	…
CH…O	**H70...O3**		0.930	…	3.084	124.51	…	…
			7.DMSO					
CH…π	**H35...π** (Cg: **10 atoms**)		0.930	2.561	3.488	173.99	3.32	173.99
	H39...π (Cg: **10 atoms**)		0.930	2.773	3.589	148.33	4.47	148.33
	H40...π (Cg: **10 atoms**)		0.931	2.800	3.444	127.26	2.78	127.26
CH…O	**H12/H64...O2**	H12...O2	0.930	2.580	3.452	156.33	…	…
	(Bifurcated)	H64...O2	0.930	2.595	3.427	149.16	…	…
	H32/H45...O3	H32...O3	0.930	2.491	3.337	151.39	…	…
	(Bifurcated)	H45...O3	0.930	2.520	3.197	129.81	…	…
	H32...O7		0.930	2.511	3.306	143.63	…	…
	H19/H68a...O4	H19...O4	0.971	2.655	3.558	154.86	…	…
	(Bifurcated)	H68a...O4	0.970	2.528	3.458	160.67	…	…
	H57...O4		0.929	2.588	3.398	145.90	…	…
O…S	**O9…S1**		…	…	3.277	…	…	…
			7.MDC					
CH…π	**H18...π** (Cg: C1-C6)		0.949	3.240	3.913	129.53	25.45	129.53

	H25...π (Cg: C14-C19)		0.950	2.991	3.811	145.26	7.56	145.26
	H26...π (Cg: C19C20N2)		0.951	2.745	3.517	139.04	11.9	139.04
CH…O	**H11B...O1/O**	H11B...O1	0.990	2.632	3.434	138.23	…	…
	3 (Bifurcated)	H11B...O3	0.990	2.543	3.328	136.24	…	…
	H11A...O2		0.990	2.462	3.393	156.64	…	…
π…π	**π...π** (Cg1: C8 C13 C12 C11 C10 C9, Cg2: 9 atoms)		…	…	3.586	…	…	…
Cl…O	**Cl2…O3**		…	…	3.161	…	…	…

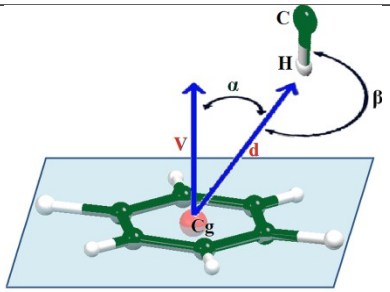

Figure S17. Protocol for CH...π interactions: d is the distance between the phenyl ring centroid (Cg) and the H atom; V is the vector normal to the plane of phenyl ring; α is the angle between the d and V vector, and β is the C–H...Cg angle.

For instance, the intermolecular interactions H61...*π*, H49...*π* (**5**) and H39...*π* (**7**.*DMSO*) lead to the formation of infinite 1D helical chain with helical pitch 28.963Å and 28.822 Å, respectively (which is equivalent to its unit cell parameter *c*). A representative view is provided in Figure S18a for **7.**DMSO (Other views are depicted in Supporting Information, Figure S19-S21). The presence of *N*-naphthyl substituents in **6** alters the packing pattern and indeed forms, infinite 1D saw shape molecular stacking along the *b*-axis involving H6...*π* or H15...*π* and *π*...*π* interactions. (Figure S18b) Mutually all the noncovalent interactions in **5**, **6** and **7**.*DMSO* lead to the formation of an infinite 3D molecular network consisting of voids occupied by corresponding solvent molecules, that are translated in infinite channels as shown in Figure S18c-e. In case of **7**.CH_2Cl_2, solvent molecules played a crucial role in directing the crystal packing patterns of this molecule. For instance, π...π and Cl...O interactions lead to an attractive helical arrangement along c axis, however, all these noncovalent interactions mutually leads to the formation of a 3D infinite supramolecular assembly consisting relatively smaller voids occupied by CH_2Cl_2 molecules, compared to **7**.DMSO. Moreover, the two closing π...π interactions involve half of the linker moiety of two molecules which oriented adjacent molecule in *anti* fashion. Notably, differential stereoelectronic factors associated with CH_2Cl_2 molecules have efficiently tuned the noncovalent interactions, involving CH_2Cl_2 molecules in CH...O interactions that together with effective CH...π, π...π interactions have resulted into the formation of unique 3D interlocked undulated architecture as illustrated in Figure S18f.

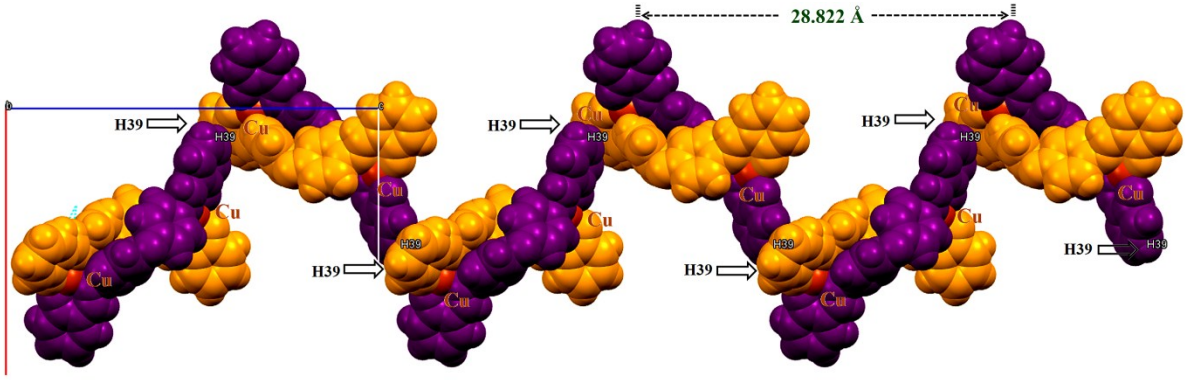

(a)

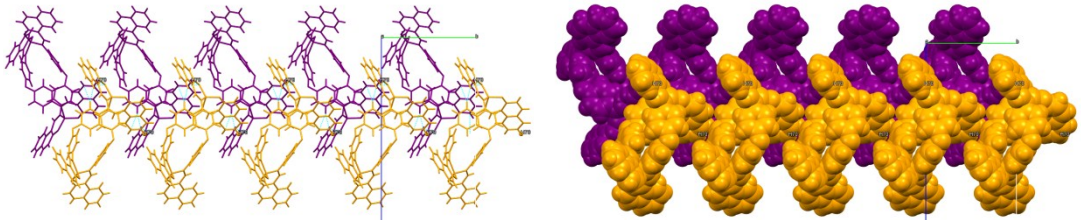

(b)

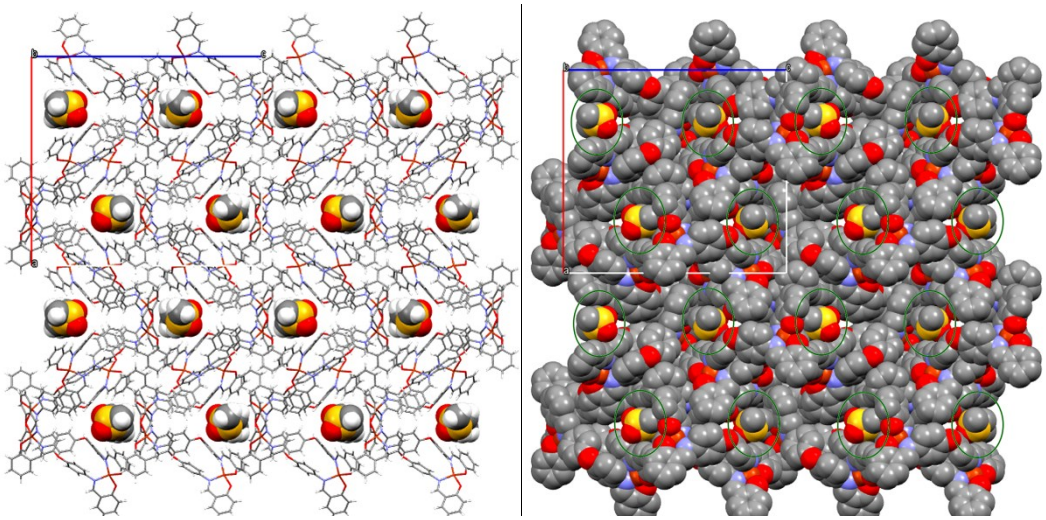

(c)

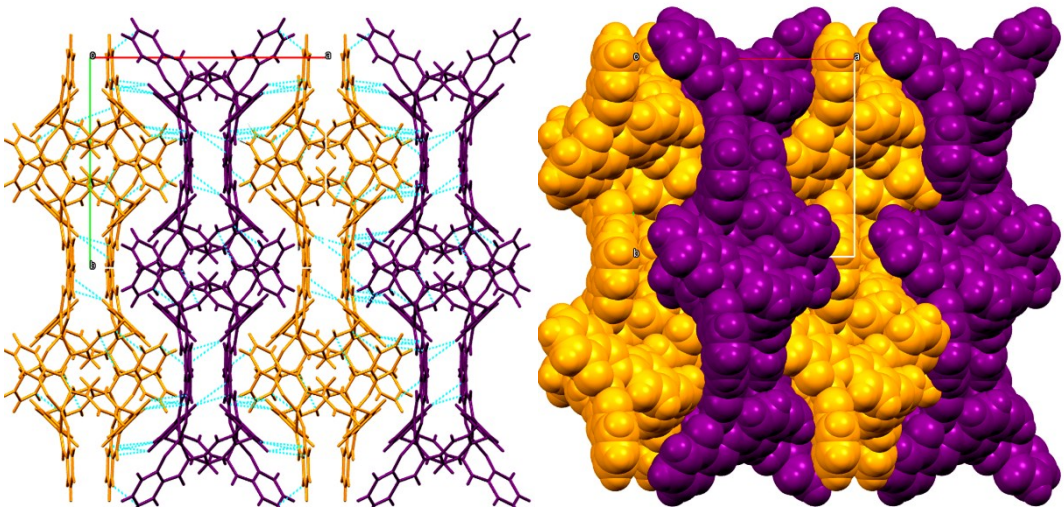

(d)

Figure S18. (a) CH...π interactions forming infinite 1D helical chain, (b) packing pattern illustrating an infinite 1D saw shape molecular stacking, (c) 3D supramolecular assembly formed through noncovalent interactions capped stick and spacefill model (H are omitted for clarity) a view along the *b*-axis (2.2.2) for **7.DMSO** (d) Formation of 3D infinite interlocked undulated architecture through noncovalent interaction in **7**.CH_2Cl_2.

Other packing patterns:

5*:* Interestingly, the **H61...π** (Cg: C49 C59 C57 C52 C33 C55) interactions can be used to generate 1D infinite helicate along *b*-axis whereas **H49...π** (Cg: C35 C11 C13 C20 C54 C42) interactions forms another helicate along *c*-axis, with helical pitch 28.963 Å (Figure S19). The **H24...π** (Cg: C22 C60 C53 C46 C63 C44) interactions are associated with two CH...O interactions viz. **H8...O5/O15** and **H21...O15**, which are closing contact, hence forms macrocyclic assembly.

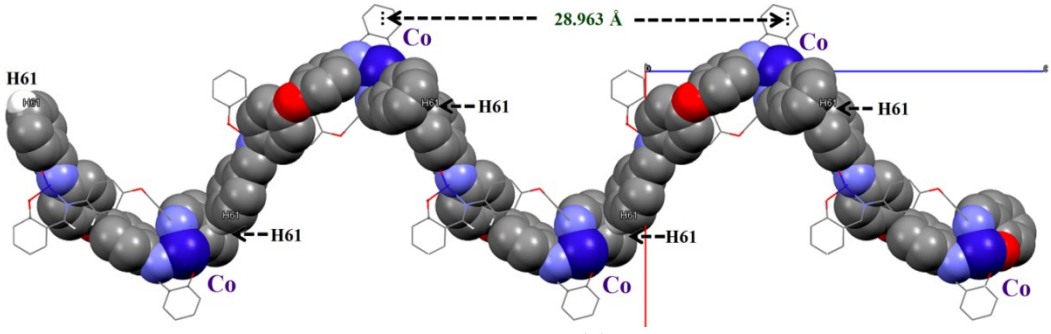

(a)

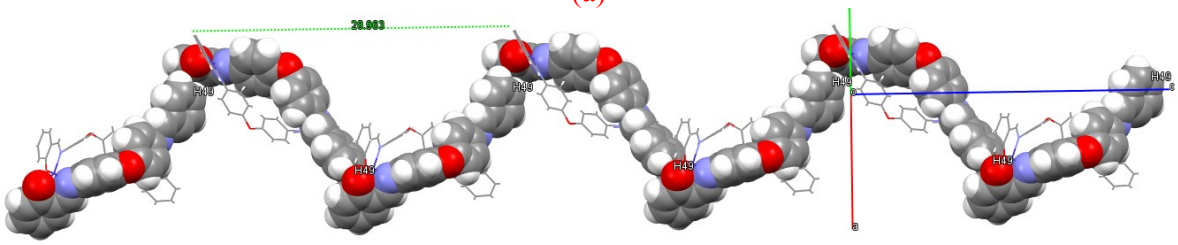

(b)

Figure S19. (a) and (b) Formation of helicates along b- and c-axis through noncovalent interactions.

***6**:* The H21...π(Cg: N4 C59 C60) donor-acceptor interactions are closing contact which holds two molecules exactly in *anti* manner and are associated with **H61...π** interaction, which leads to the formation of two molecular finite '*S-shaped*' self-assembly. Additionally, 1D wavy arrangement along *c*-axis and 1D stacking along *a*-axis have been formed through **H42...π** and **H42...π** interactions, respectively. (Figure S20 a-b) Four double helical macrocyclic molecular units are situated at four diagonal corners of the unit cell of **6** whereas dimenstionality is extended predominantly through CH...π and CH...O interactions to the formation of infinite 3D architecture consisting of number of voids.

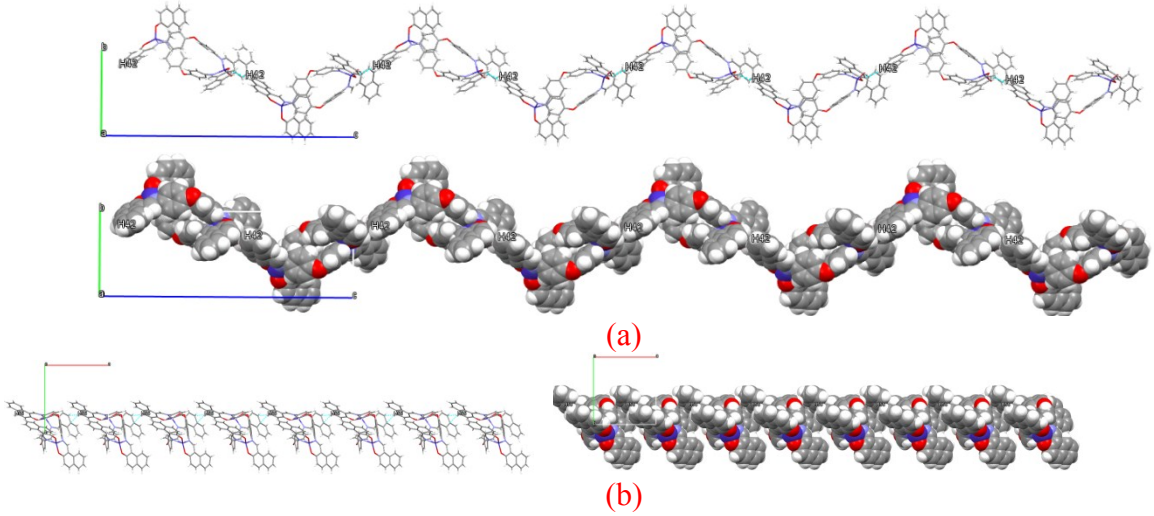

Figure S20. (a-b) Formation of 1D wavy arrangement along *c*-axis and 1D stacking along *a*-axis have been formed through **H42...π** and **H42...π** interactions, respectively.

7.*2*CH_2Cl_2*:* The **π...π** interactions align molecules in *anti* and lead to 1D packing (Figure 21a) and Cl...O interactions in cooperation with CH...O interactions, pack the molecules in *ac* plane *via* dichloromethane (Figure 21b). Notably, distinct crystal packing pattern is observed when DMSO is switched over to CH_2Cl_2, for instance smaller voids are generated due to crystal packing which are occupied by CH_2Cl_2 molecules. Hydrogen of CH_2Cl_2 molecules are also involved in CH...O interactions with both the chelated phenolic oxygens of either side.

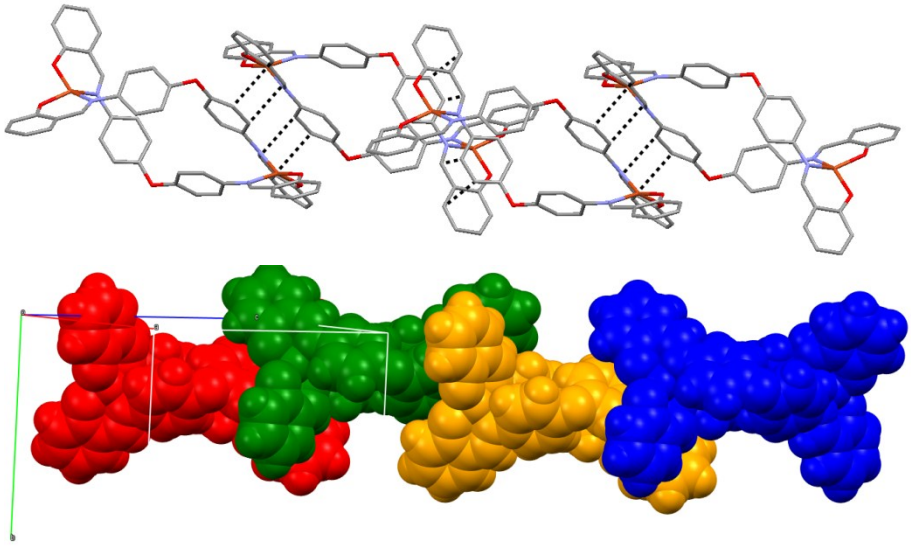

(a)

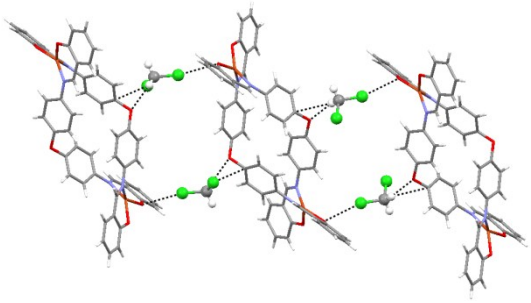

(b)

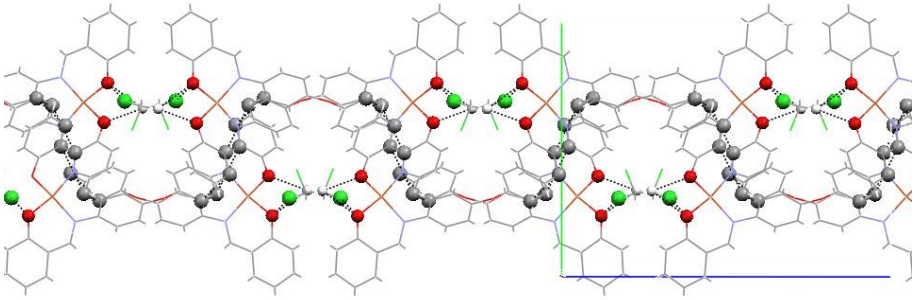

(c)

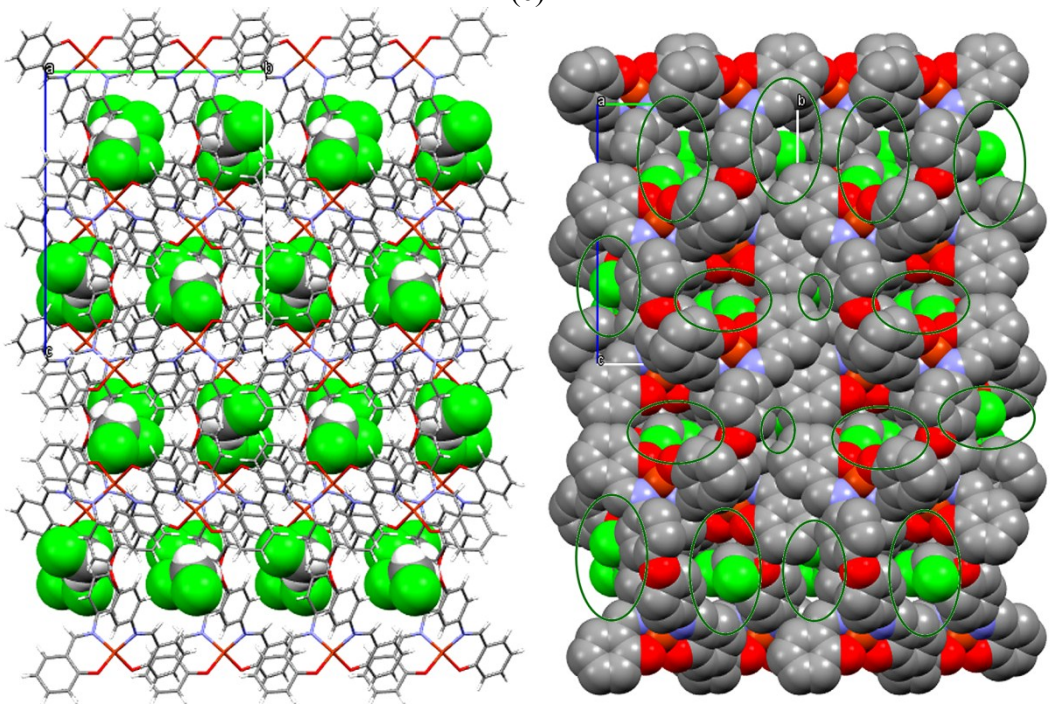

(d)

Figure S21. (a) View of the layer formed by the $\pi\ldots\pi$-stacking interactions (b) Molecular packing in *ac* plane *via* dichloromethane molecules. (c) Helical chain-like packing along the c-axis. (d) Molecular packing view along *a*-axis (2.2.2) in complex **7**.CH_2Cl_2, H atoms and solvent molecules were omitted for clarity.

UV-visible absorption and Emission. The UV–visible absorption (10^{-4} M) and emission (10^{-4} M) property of ligand precursors (**L** [1], **L** [2]), potassium salt of xanthate ligands (**K_2xan**[1], **K_2xan** [2]), binuclear xanthate macrocyclic complexes (**1–4**) as well as binuclear *N,O*-Schiff base macrocyclic complexes **(5-8)** were investigated at room temperature from DMSO solution

samples. The differential electronic spectra of **1-8** shown in Figure S22a-b clearly suggest alterations in the structural features of the molecular framework. The shorter absorption band ~315 nm is assigned to π→π* (phenyl) transitions and the longer absorption band ~360 nm is assigned to n→π* (imine) transitions while the absorption band in the range of 390-490 nm could be attributable to the intraligand charge transfer in respective compounds.

It appears that the λ_{max} value for all the compounds arises due to phenyl π→π* transitions do not show any significant change with the change in the functionality. As expected, the band due to imine n→π* transitions appeared in ligand precursors $\mathbf{L^1}$, $\mathbf{L^2}$ remains unaffected in corresponding xanthate ligands $\mathbf{K_2xan^1}$, $\mathbf{K_2xan^2}$ and bimetallic xanthate complexes **1-4**, however a distinguishable blue shift of 10-15 nm in **5-8** as compared to the similar transitions observed in $\mathbf{L^1}$ and $\mathbf{L^2}$, clearly underlines the participation of imine moiety in complex formation. Further ligand precursors $\mathbf{L^1}$, $\mathbf{L^2}$ display strong bands due to charge transfer transitions at 395 and 480 nm respectively, predominantly arises due to the presence of phenolic hydroxyl moiety present in conjugation with imine (–CH=N-) functionality. These bands significantly shifted towards higher wavelength *ca* 444 nm and 490 nm upon formation of $\mathbf{K_2xan^1}$, $\mathbf{K_2xan^2}$ ligands respectively. These bands undergo substantial blue shifts upon complexation with metal ions. For instance a hefty blue shift of 39 nm (**1**), 57 nm (**2**) and 29 nm (**4**) has been observed. In contrast a minor red shift of approx 8 nm in the charge transfer transition band (444 nm) of $\mathbf{K_2xan^1}$ ligand is observed upon comlexation with Cu^{II} ion. In addition to these transitions, all complexes 1-8 exhibit a weak d-d transition bands in the visible region of the spectrum. The cobalt complexes **1-2** and **5-6** displayed a weak absorption band in the range of 531- 565sh nm suggesting distorted tetrahedral geometry around the Co^{II} centers whereas copper complexes **3-4** and **7-8** displayed a weak band in the range of 670- 690 nm suggesting distorted square planar / tetrahedral geometry around the Cu^{II} centers.

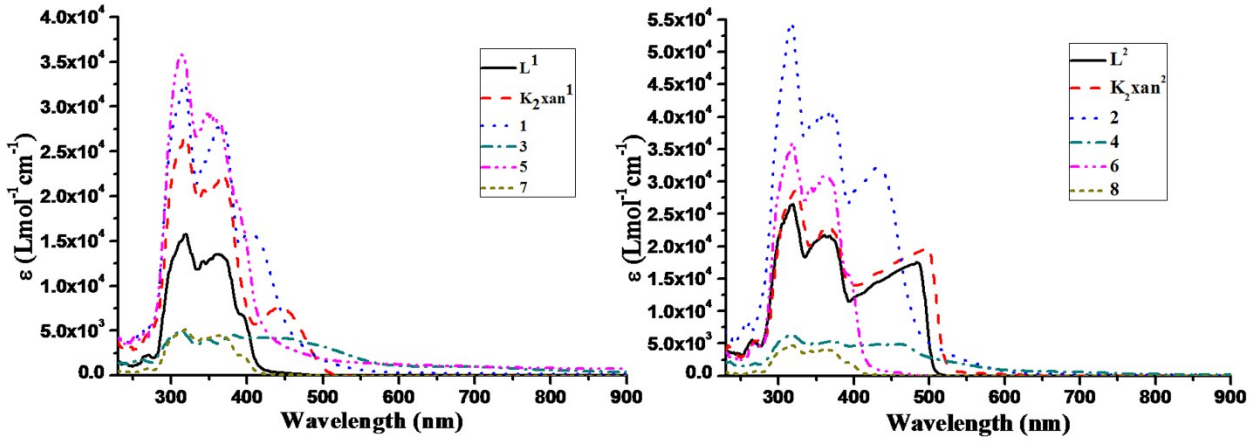

(a) (b)

Figure S22. UV-visible absorption spectra of Schiff base precursors, xanthate salts, binuclear xanthate complexes and binuclear Schiff base complexes at room temperature in 10^{-4} M DMSO solution: (a) $\mathbf{L^1}$, $\mathbf{K_2xan^1}$, **1**, **3**, **5** and **7**; (b) $\mathbf{L^2}$, $\mathbf{K_2xan^2}$, **2**, **4**, **6** and **8**.

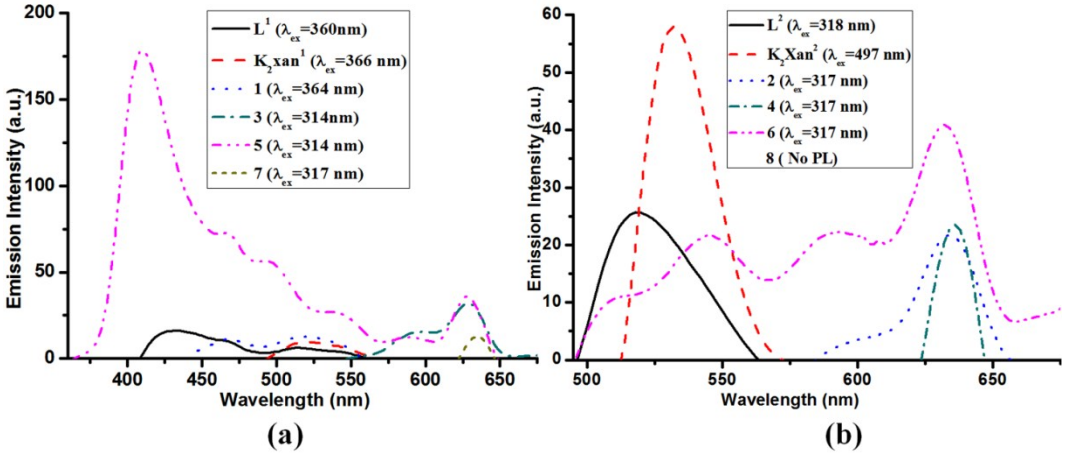

Figure S23. Fluorescence spectra of Schiff base precursors, xanthate salts, binuclear xanthate complexes and binuclear Schiff base complexes at room temperature in 10^{-4} M DMSO solution: (a) **L**[1], **K**$_2$**xan**[1], **1**, **3**, **5** and **7**; (a) **L**[2], **K**$_2$**xan**[2], **2**, **4**, **6** and **8**.

The fluorescence spectra of ligand precursors (**L** [1], **L** [2]), potassium salt of xanthate ligands (**K**$_2$**xan** [1], **K**$_2$**xan** [2]), binuclear xanthate macrocyclic complexes (**1-4**) as well as binuclear *N,O*-Schiff base macrocyclic complexes **(5-8)** shown in Figure S23, clearly suggests that **L** [1] and **K**$_2$**xan**[1] display very weak intensity band at 432, 513 and 520 nm at λ_{ex} 360 and 318 nm respectively however **L**[2] and **K**$_2$**xan**[2] display very strong bands 519 and 532 nm at λ_{ex} 318 and 497 nm respectively with a significant Stokes shift. Besides the Co^{II} N, O-Schiff base complex **5** is found to be highly fluorescent, display a high sharp intensity 410 nm at λ_{ex} 314 with a Stokes shift of ≈ 138 nm. As copper (II) is generally a fluorescence quencher, all the Cu^{II} complexes display no significant fluorescence properties. The observed trend of fluorescence spectra and concomitant bathochromic shifts of intramolecular charge-transfer emissions by coordination compounds were previously observed in dithiocarbamate[4], dialkoxo-bridged[5] and Salen-type[6] complexes. The appearance of more number of bands upon excitation of a single wavelength as well as high fluorescence behaviour of the complexes may be attributed to the reduction of photoinduced electron transfer process on complex formation.[7] In conclusion the results of emission study suggest that the emission intensities are dependent on not only on the extended conjugation but also on rigidity in the molecule, which suppresses the distortion of the molecular framework and the concomitant nonradioactive decay process.

Theoretical Investigations. All calculations were performed with the Gaussian 03 program suite.[8] The geometry for all the model compounds discussed herein was fully optimized (Figure S24) by density functional theory at the DFT B3LYP/lanl2dz level. Such type of basis set has been used with good success in a number of studies involving similar species, having good agreement with experimental results.[9] Molecular orbitals were generated using GaussView 3.0 program.

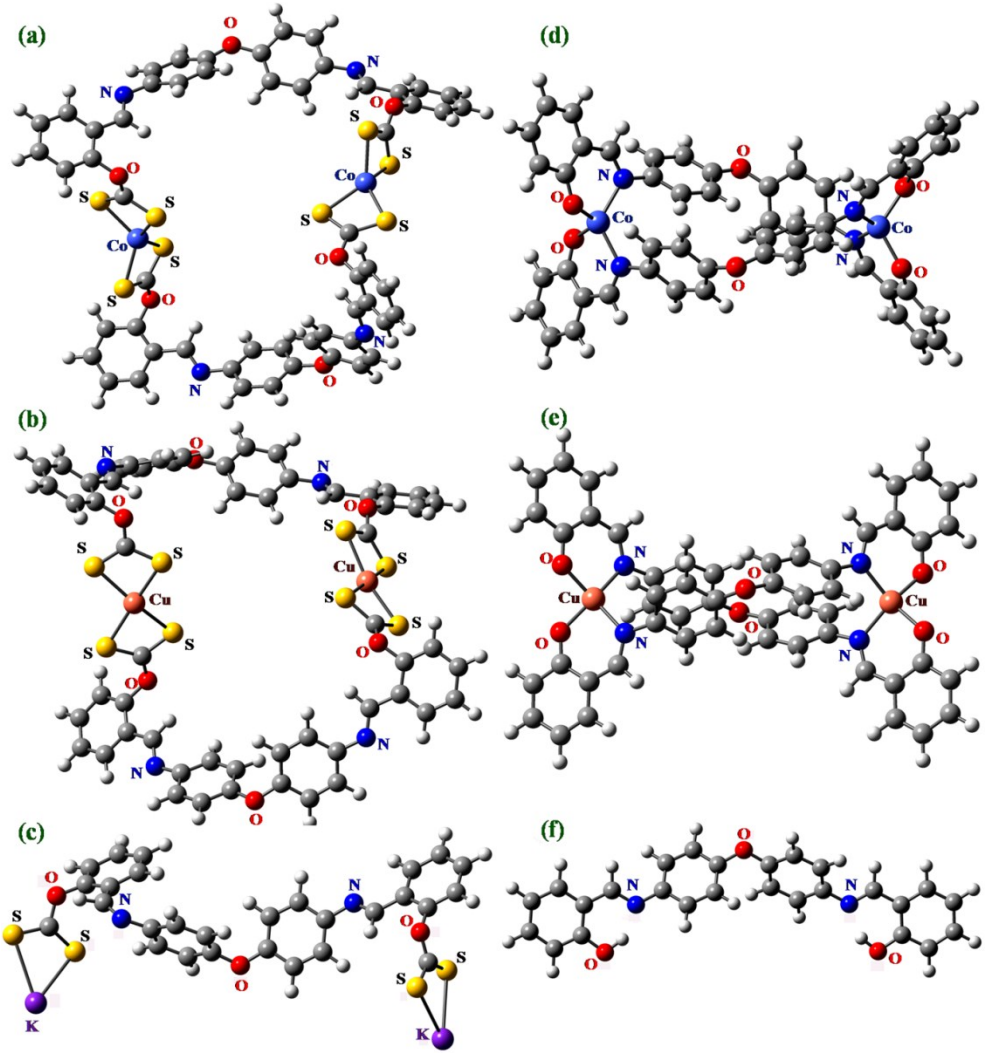

Figure S24. An optimized geometry for the minimum energy conformation at B3LYP/lanl2dz level for **1** (a), **2** (b), **Kxan-1** (c), **5** (d), **7** (e), $\mathbf{L_1}$ (f).

The outcomes of theoretical study are in good agreement with the experimental data. The flexibility associated with the linker along with the desired orientations of xanthate moieties of K_2xan[1] is essentially the key factor involved in the macrocyclization process, leading to binuclear complexes **1-4**. It appears that the optimized structures adopt a unique orientation to diminish the steric and electronic factors associated with them. For instance, boat shaped macrocyclic architectures are obtained as a lower energy conformation in case of binuclear xanthate complexes **1** and **3**, whereas double helical macrocyclic architectures are obtained for binulear *N, O*-Schiff base complexes 5 and 7. These architectures are exemplified in Figure S25-S26.

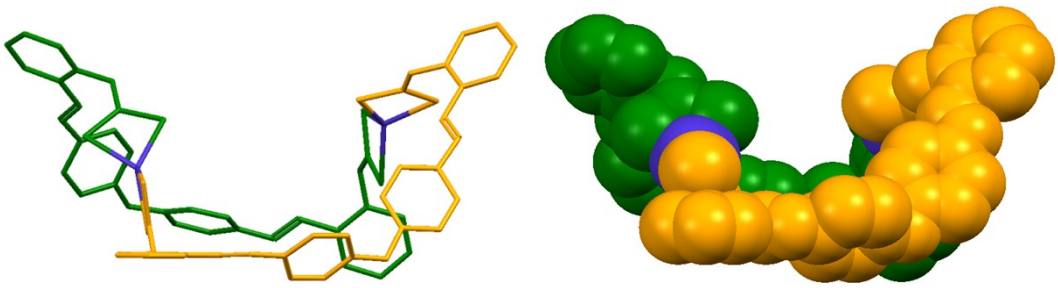

(a) (b)

Figure S25. Complex **1** forming boat shaped macrocyclic architecture represented by capped sticks (a) and spacefill (b) models.

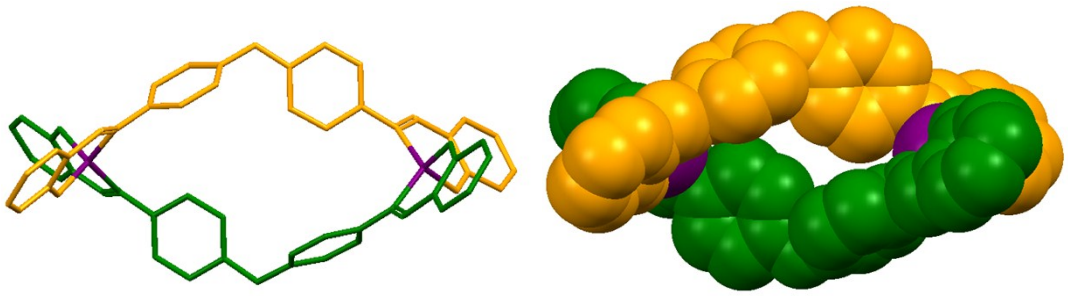

(a) (b)

Figure S26. Complex **5** forming double helical macrocyclic architecture represented by capped sticks (a) and spacefill (b) models.

An optimized geometry of complexes **1**, **5** and **7** suggests distorted tetrahedral coordination sphere at both the metal centers however complex **3** adopts distorted square planar geometry around both the Cu^{II} centers. The geometrical parameters of the binuclear *N, O*-Schiff base macrocyclic complexes **5** and **7** are well compared with their experimental parameters obtained from single crystal X-ray study (Table S3) and these validate the optimized electronic structural models of compounds under investigation. The small difference between the geometrical parameters obtained theoretically and from X-ray crystallography of compound **5** is probably emerged due to the presence of large number of non-covalent interactions offered by the spacer moiety intending an extra stability to the macrocyclic architecture.

Table S5. Selected structural parameters obtained from theoretical investigations and X-ray study for**1**, **3, 5** and **7**.

Entry	Selected Bond	Bond Length (Å)		Selected Bond	Bond Length (Å)	
		Theoretical	X-ray		Geometrical	X-ray
5	O–Co	1.917, 1.921	1.890, 1.900, 1.906, 1.884	O–Co–N	94.08, 94.54	94.62, 95.29, 93.46, 91.71
	N–Co	2.047, 2.043	1.991, 1.953, 1.972, 1.985	O–Co–O	117.61	94.24, 91.07
	N–C (imine)	1.312, 1.309	1.284, 1.288, 1.301	N–Co–N	123.70	101.00, 101.29
	O–C (ether)	1.387, 1.381	1.381, 1.396, 1.384, 1.379	C–C–N	128.16, 128.43	127.14, 127.68, 126.35, 126.88
	Co_1–Co_2	11.259	11.750	C–N–Co	118.64, 118.65, 119.32	122.70, 121.61, 122.85, 121.95
				C–O–Co	124.93, 126.49	126.75, 127.47, 124.63, 128.86
				C–O–C (ether)	118.88	115.42, 117.92
7	O–Cu	1.930	1.888, 1.893	O–Cu–N	93.33	94.11-94.92
	N–Cu	2.029	1.957, 1.976	N–Cu–N	104.34	98.12
	N–C	1.421	1.299-1.434	O–Cu–O	96.22	92.80
				N–Cu–O	139.48-139.53	145.29-145.89
				C–C–N	128.20	125.87-126.82
				C–N–Cu	122.10-122.11	121.48-122.76
				C–O–Cu	128.84-128.85	123.16-127.69
				C–O–C	118.32	115.91

Table S6. Computational calculation data for complex **1**, **3, 5, 7**

Sr.	Entry	Energy (10^6 Kcal/mol)	HOMO-LUMO Band gap (eV)	Theoretical λ_{max} value (experimental λ_{max} value) nm
1	**1**	-3.9543	3.4645	358 (366)
2	**3**	-4. 0184473	3.3941	365 (380)
3	**5**	-1.8599	3.5688	347 (349)
4	**7**	-1.9238968	3.6303	342 (359)

Frontier molecular orbital analysis. The character of the frontier orbitals and the HOMO–LUMO energy gap greatly contribute to the photo-physical properties of the complexes and thus analysis of frontier molecular orbitals need prime consideration for prediction of the possible reactivity of the molecule.[10]

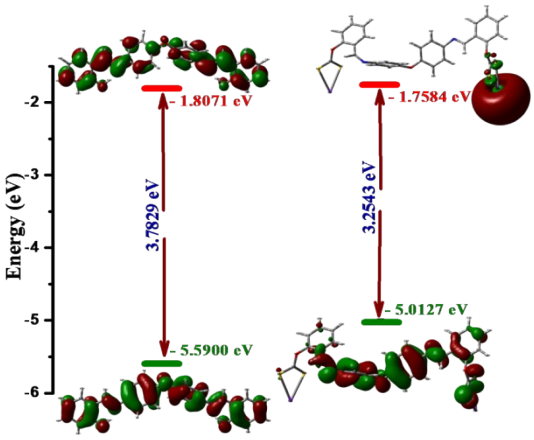

(a)

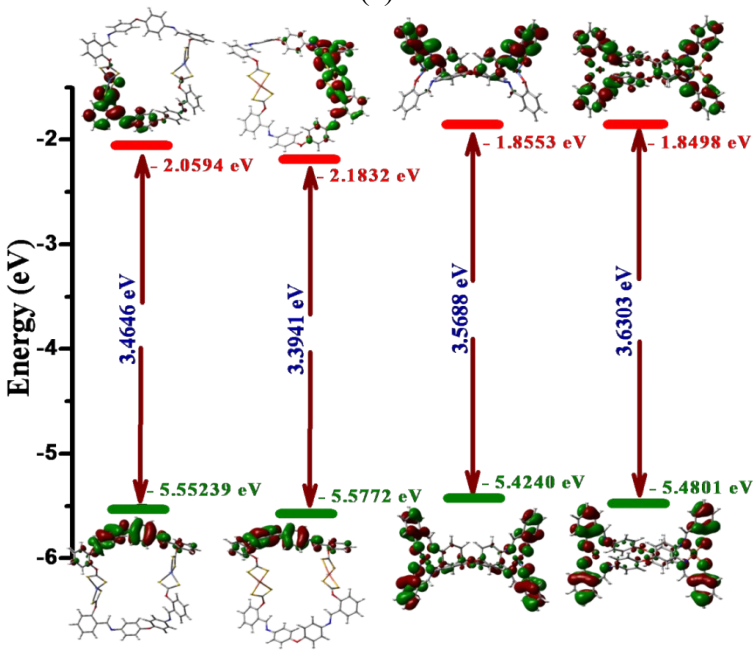

(b)

Figure S27. Comparison of the frontier molecular orbitals derived from DFT calculation at the B3LYP/LAN2DZ level; for (a) $\mathbf{L_1}$ and **Kxan-1**, (b) **Complexes 1**, **3**, **5** and **7**.

Due to the effective conjugation, HOMO and LUMO in $\mathbf{L^1}$ are delocalized over all the phenyl rings whereas HOMO of $\mathbf{K_2xan^1}$ is mainly delocalized over phenyl rings adjacent to ethereal

oxygen and to a little extent to the xanthate moieties. Expectedly, LUMO of **K_2xan[1]** is mainly localized over a xanthate moiety and potassium attached to xanthate as illustrated in Figure S26a. The electron density in the HOMO for binuclear xanthate complexes **1** and **3** is predominantly delocalized over the phenyl moieties adjacent ethereal with oxygen, while metal chelated xanthate moieties are mainly contributed for LUMO as shown in Figure S27b. The transformation of the binuclear xanthate complexes to their corresponding binuclear *N,O*-Schiff base analogues can be explained by the localization of LUMO at metal chelated xanthate moiety in complexes **1** and **3** which emphasizes the vulnerability of xanthate moiety under nucleophilic conditions. The HOMO for **5** and **7** is predominantly delocalized over spacer moiety; the π-orbitals of two peripheral phenyl moieties of linker unit are commonly contributing to the high extent for the delocalization of the HOMO. However, the LUMO in **5** is mainly delocalized over the length of the one of the ligand portion and it is delocalized over peripheral phenyl moieties in **7** with minor contribution by the phenyl moieties attached to ethereal oxygen as shown in Figure S27b. On the other hand, for both the compounds the contribution from the metal atom in their HOMOs and LUMOs is extremely negligible. Thus, frontier molecular analysis suggests that the chelated xanthate moiety can preferentially react with nucleophilic species and all the complex molecules can show an efficient CH-π and π-π donor-acceptor ability.

Furthermore, the significant decrease in the energy difference between HOMO-LUMO is observed upon reaction of **L_1** (3.7829 eV) with CS_2 leading to the **Kxan-1**(3.2543 eV), due to higher electron density and extended conjugation. We have also found that the energies of HOMO and LUMO of **1**and **3** are lower than that of **5** and **7**, energy difference between HOMOs is smaller but LUMOs are greatly differentiated by energy. The energy difference between HOMO-LUMO for xanthate complexes (3.4646 eV for **1** and 3.3941 eV for **3**) is significantly lower compared to their corresponding Schiff base complexes (3.5688 eV for **5** and 3.6303 eV for **7**), could be due to the presence of flexible skeletal structures of the xanthate ligand. Additionally, this study also revealed the greater contribution of copper towards decrease of the HOMO-LUMO energy difference in xanthate complexes in spite of identical molecular framework except metal centers, however reverse trend is observed in Schiff base complexes. The lower energies of HOMO in copper containing complexes (**3** and **7**) over their cobalt centered congeners (**1** and **5**) also suggest their superior stability. Interestingly, the HOMO–LUMO energy gap values for the entire investigated compound are in the range of 3.38-3.79 eV which reveals the possible semiconducting properties of the compounds[11] and increases the potential applicability of this class of compounds towards semiconducting materials.

The electrostatic potential (ESP) of molecules are widely used as a powerful tool for exploring the properties and locating potential sites within the molecules for the interactions with other moieties and thus it provides insights into molecular association. For instance, the surface property of drug molecule reveals the potential sites of interactions with biomolecules which is useful to estimate the mode of action.[12]

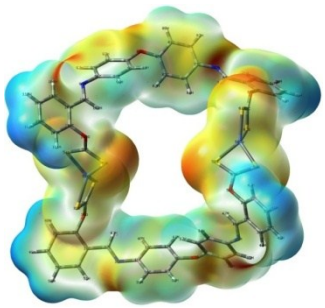

(a)

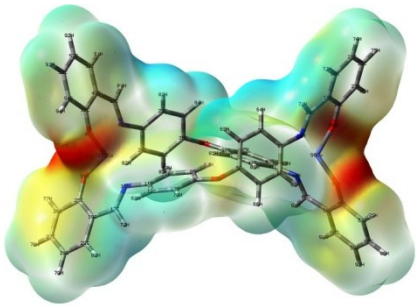

(d)

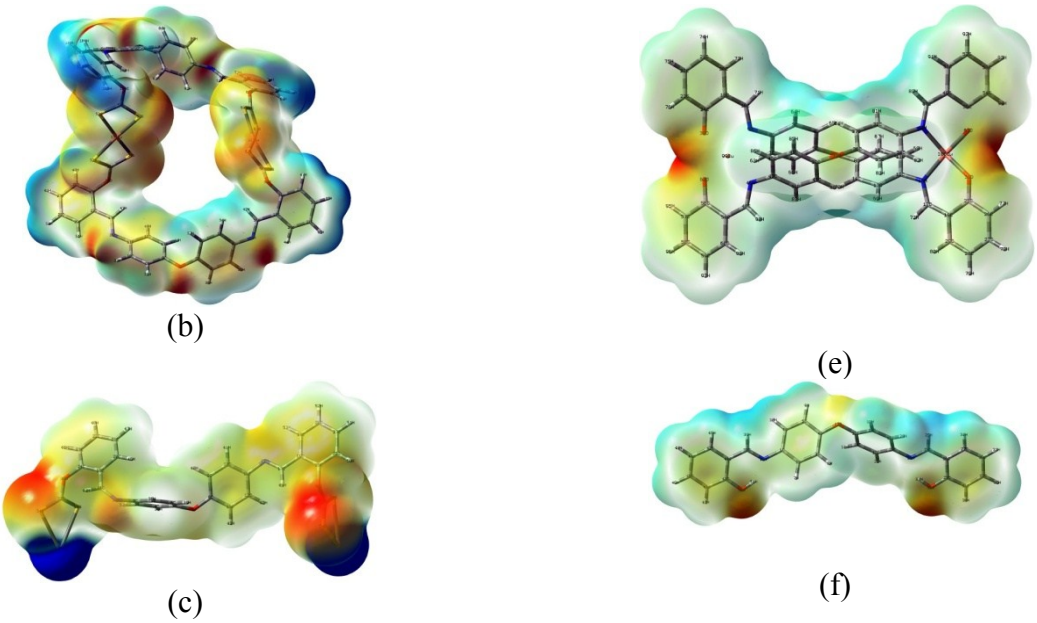

Figure 28. Graphical representation of electron density from total SCF density (isoval= 0.0004; mapped with ESP) for **a-f:** Complex **1**, **3**, **K_2xan[1]**, **5**, **7** and **L^1** respectively **(**Red color indicates negative potential whereas blue color indicates negative potential)

The localization of slight negative potential around –OH in **L^1** and very high positive potential around potassium centers and quite negative potential around sulfur atoms in **K_2xan[1]** can be clearly seen in Figure S28. Furthermore, the localization of low positive potential at aromatic hydrogen atoms moderately negative potential around N/O/S in macrocyclic complex **1** (a), **3** (b), **5** (d) and **7** (e) could be clearly revealed from mapping of electrostatic potential surface (Figure S28). This has indeed generated a scope for the use of these macrocyclic complexes with variable cavity size and tuneable electronic environment as ditopic receptors to interact with suitable guest species (*vide supra*). Gejji et al. have depicted the exploitation of molecular electrostatic potential from density functional calculations to understand the host-guest interactions.[13] In this context, the surface potential of binuclear xanthate macrocyclic complexes **1** and its Schiff base analogue **5** clearly explain the sensing ability of various metal ions using fluorescence spectroscopy (*vide supra*).

Cartesian Coordinates for Optimized Geometries:

Table S7. Cartesian coordinates for optimized geometry of **L^1**.

Atom Type	Coordinates (Angstroms)		
	X	Y	Z
C1	-3.7405	-0.4649	-0.0461
C2	-2.6694	0.1024	-0.7552
C3	-1.4117	-0.4908	-0.7533
C4	-1.2009	-1.6536	-0.005
C5	-2.2468	-2.2178	0.7284
C6	-3.5068	-1.6287	0.7073
H7	-2.8466	1.0061	-1.3295
H8	-0.5987	-0.0557	-1.3237
H9	-2.0535	-3.1081	1.3172
H10	-4.3027	-2.053	1.3111
O11	0	-2.3351	5.00E-04
C12	1.2008	-1.6536	0.0057
C13	2.2464	-2.2174	-0.7286
C14	1.4121	-0.4913	0.7547
C15	3.5064	-1.6283	-0.7078
H16	2.0527	-3.1073	-1.3179
C17	2.6698	0.1018	0.7564
H18	0.5993	-0.0567	1.3257
C19	3.7405	-0.465	0.0464
H20	4.302	-2.0523	-1.3122

H21	2.8473	1.0051	1.3312
N22	-4.9824	0.1937	-0.0983
N23	4.9824	0.1935	0.0986
C24	6.0977	-0.4558	0.0063
H25	6.1152	-1.5513	-0.0585
C26	7.3825	0.2127	1.00E-03
C27	8.5684	-0.5434	-0.0913
C28	7.4751	1.6311	0.0906
C29	9.8128	0.066	-0.1
H30	8.489	-1.626	-0.1574
C31	8.7397	2.2401	0.0813
C32	9.888	1.4652	-0.0131
H33	10.7169	-0.5291	-0.1726
H34	8.7878	3.3216	0.1499
H35	10.8585	1.9533	-0.0189
O36	6.3868	2.4066	0.186
H37	5.5945	1.8004	0.1838
C38	-6.0977	-0.4556	-0.0068
H39	-6.1151	-1.5513	0.0571
C40	-7.3825	0.2127	-0.0015
C41	-7.4751	1.6312	-0.0905
C42	-8.5684	-0.5434	0.09
C43	-8.7397	2.2402	-0.0814
C44	-9.8128	0.066	0.0986
H45	-8.489	-1.6261	0.1558
C46	-9.888	1.4651	0.0122
H47	-8.7878	3.3217	-0.1495
H48	-10.7169	-0.5292	0.1707
H49	-10.8584	1.9533	0.0178
O50	-6.3868	2.4067	-0.1852
H51	-5.5944	1.8004	-0.1828

Table S8. Cartesian coordinates for optimized geometry of **K_2xan[1].**

Atom Type	Coordinates (Angstroms)		
	X	Y	Z
C1	-2.7085	-0.3078	1.9865
C2	-3.9232	-0.3429	1.2809
C3	-3.9036	-0.6868	-0.083
C4	-2.6963	-0.9545	-0.7245
C5	-1.4947	-0.8801	-0.0174
C6	-1.4988	-0.5579	1.3436
O7	-0.3375	-1.2341	-0.6911
C8	0.8113	-0.4818	-0.5512
C9	0.8039	0.906	-0.3694
C10	2.0109	1.5963	-0.3189
C11	3.2418	0.9264	-0.4215
C12	3.227	-0.4658	-0.6305
C13	2.024	-1.1624	-0.6929
N14	-5.1217	-0.167	2.0009
N15	4.4105	1.7035	-0.3612
C16	-6.0743	0.6061	1.634
C17	5.4884	1.2097	0.1309
C18	-6.1365	1.6125	0.545
C19	6.7423	1.9706	0.158
C20	-5.0451	2.4193	0.1834
C21	-5.1785	3.4139	-0.7825
C22	-6.4103	3.6213	-1.4099
C23	-7.5101	2.837	-1.0649
C24	-7.3643	1.8489	-0.0969
C25	7.9204	1.396	0.6628
C26	9.1157	2.1077	0.7176
C27	9.1532	3.4191	0.249
C28	7.9954	4.0126	-0.2687
C29	6.8063	3.2951	-0.3115
O30	-8.4997	1.1594	0.3189
O31	7.8697	0.126	1.2375
C32	-8.77	-0.1227	-0.0829
C33	8.1993	-1.0066	0.5455
S34	-10.0991	-0.7902	0.7496
S35	8.648	-0.8784	-1.0994
H36	-2.7279	-0.0825	3.0488
H37	-4.8395	-0.7411	-0.6321

H38	-2.6707	-1.2216	-1.7767
H39	-0.5644	-0.5226	1.8947
H40	-0.1378	1.4374	-0.2827
H41	2.0231	2.6745	-0.1904
H42	4.1628	-0.9995	-0.7686
H43	2.0039	-2.2348	-0.8622
H44	-6.9877	0.5383	2.2304
H45	5.5237	0.2074	0.5714
H46	-4.0919	2.2696	0.6788
H47	-4.324	4.0329	-1.0404
H48	-6.5165	4.3958	-2.1643
H49	-8.4799	2.9777	-1.5306
H50	9.9972	1.6253	1.1266
H51	10.084	3.9783	0.2897
H52	8.0244	5.0361	-0.6322
H53	5.8952	3.7355	-0.7029
S54	8.0708	-2.4072	1.5145
S55	-7.8095	-0.8336	-1.3073
K56	8.8309	-3.9498	-1.0312
K57	-9.019	-3.4763	-0.2867

Table S9. Cartesian coordinates for optimized geometry of **1**.

Atom Type	Coordinates (Angstroms)		
	X	Y	Z
C1	1.592	-6.1422	0.376
C2	2.7961	-6.8636	0.2955
C3	2.995	-7.7113	-0.8088
C4	2.0488	-7.7993	-1.822
C5	0.8636	-7.0599	-1.7327
C6	0.6306	-6.2356	-0.6271
O7	-0.0098	-7.174	-2.7936
C8	-1.3414	-6.8326	-2.6265
C9	-2.1611	-7.5362	-1.7373
C10	-3.5114	-7.2172	-1.6536
C11	-4.0558	-6.1768	-2.4274
C12	-3.2229	-5.5015	-3.3372
C13	-1.8718	-5.8285	-3.4362
N14	3.8014	-6.8249	1.2769
N15	-5.4257	-5.9053	-2.2725
C16	4.0067	-5.7477	1.9418
C17	-5.8563	-4.7012	-2.3583
C18	4.9944	-5.6912	3.0275
C19	-7.2895	-4.3941	-2.2558
C20	5.7226	-6.8277	3.4236
C21	6.6384	-6.7634	4.4674
C22	6.8432	-5.5607	5.1535
C23	6.1346	-4.4178	4.7849
C24	5.2376	-4.4999	3.7266
C25	-7.7576	-3.0731	-2.281
C26	-9.1089	-2.7542	-2.2088
C27	-10.038	-3.7859	-2.0861
C28	-9.6052	-5.1164	-2.0449
C29	-8.2506	-5.4143	-2.1327
O30	-6.8321	-2.0296	-2.4897
C31	-6.4163	-1.2526	-1.488
S32	-6.8671	-1.5004	0.1465
S33	-5.3726	0.0341	-1.9237
H34	1.3878	-5.5233	1.2448
H35	3.9141	-8.2869	-0.8592
H36	2.2035	-8.44	-2.6843
H37	-0.2943	-5.6754	-0.5474
H38	-1.7381	-8.331	-1.1311
H39	-4.1683	-7.757	-0.9787
H40	-3.6393	-4.7378	-3.9874
H41	-1.2215	-5.3196	-4.1406
H42	3.4595	-4.8216	1.7346
H43	-5.1819	-3.8492	-2.5016
H44	5.5411	-7.753	2.8872
H45	7.1904	-7.653	4.7568
H46	7.5504	-5.5111	5.9761
H47	6.2696	-3.4748	5.3037
H48	-9.4172	-1.7149	-2.2504

H49	-11.0964	-3.5503	-2.0261
H50	-10.3299	-5.9198	-1.9511
H51	-7.8954	-6.4391	-2.1094
Co52	-5.5005	0.4793	0.4379
S53	-3.7786	0.9756	2.0445
S54	-6.2874	2.4932	1.5214
C55	-4.8226	2.2902	2.3873
O56	4.4598	-3.3691	3.3989
C57	4.9516	-2.3603	2.6805
S58	3.8483	-1.1022	2.3097
S59	6.5734	-2.2916	2.1304
Co60	5.7798	-0.2045	1.1967
S61	6.6621	2.0157	1.4641
S62	6.2118	0.5231	-1.0752
C63	6.7562	1.9203	-0.2437
O64	7.2552	2.9927	-0.8571
C65	7.5742	2.9967	-2.2302
C66	6.8074	3.7914	-3.0925
C67	8.7151	2.3204	-2.6494
C68	5.6035	4.4983	-2.6293
C69	7.2318	3.8816	-4.4309
C70	9.106	2.4211	-3.9832
H71	9.2859	1.7366	-1.9351
N72	5.04	5.3879	-3.359
H73	5.2235	4.234	-1.6354
C74	8.363	3.2055	-4.8728
H75	6.6428	4.495	-5.1044
H76	9.9921	1.8936	-4.3235
C77	3.8381	5.9849	-2.9456
H78	8.6699	3.2869	-5.9114
C79	3.6745	7.364	-3.1655
C80	2.7693	5.2618	-2.3899
C81	2.5063	8.0088	-2.7844
H82	4.4893	7.9188	-3.6201
C83	1.5747	5.895	-2.047
H84	2.8536	4.1848	-2.2748
C85	1.4516	7.2765	-2.2248
H86	2.3787	9.0764	-2.9326
H87	0.7444	5.3142	-1.6614
O88	0.3024	7.9958	-1.9783
C89	-0.6529	7.6095	-1.0632
C90	-1.9667	7.9884	-1.3634
C91	-0.3643	6.9799	0.1517
C92	-2.9865	7.7356	-0.4559
H93	-2.1619	8.4959	-2.3025
C94	-1.4004	6.6889	1.0383
H95	0.6593	6.7314	0.41
C96	-2.7262	7.0519	0.7443
H97	-4.0061	8.0403	-0.6699
H98	-1.1712	6.2202	1.9911
N99	-3.8026	6.8228	1.6166
C100	-3.8964	5.7107	2.2459
C101	-4.9652	5.4837	3.2303
H102	-3.1945	4.8849	2.0789
C103	-5.7617	6.5441	3.6993
C104	-5.2273	4.2092	3.7505
C105	-6.7567	6.3298	4.6464
H106	-5.569	7.5334	3.2981
C107	-6.2072	3.9751	4.708
O108	-4.4189	3.1255	3.3461
C109	-6.9779	5.0461	5.1578
H110	-7.3571	7.1642	4.9967
H111	-6.3574	2.9687	5.0846
H112	-7.7476	4.8773	5.905

Table S10. Cartesian coordinates for optimized geometry of **3**.

Atom Type	Coordinates (Angstroms)		
	X	Y	Z
C1	6.299	-4.0024	1.1682
C2	7.5646	-3.7081	0.6232
C3	8.1278	-4.613	-0.2928
C4	7.4341	-5.7484	-0.6979

C5	6.1723	-6.0118	-0.1623
C6	5.6079	-5.1463	0.7819
O7	5.5602	-7.1985	-0.5191
C8	4.2686	-7.2002	-1.0019
C9	3.5694	-8.4079	-0.8975
C10	2.2942	-8.5158	-1.4378
C11	1.6749	-7.4144	-2.0549
C12	2.3992	-6.2132	-2.1625
C13	3.688	-6.1038	-1.6477
N14	8.3433	-2.5901	0.9612
N15	0.3861	-7.5989	-2.5819
C16	7.8114	-1.5045	1.3883
C17	-0.4401	-6.6185	-2.6145
C18	8.6497	-0.3609	1.7748
C19	-1.7579	-6.7467	-3.2505
C20	10.0496	-0.4046	1.6314
C21	10.8441	0.6736	2.0003
C22	10.2598	1.827	2.5369
C23	8.8777	1.8974	2.6971
C24	8.0974	0.8137	2.3044
C25	-2.6624	-5.6747	-3.2678
C26	-3.8947	-5.742	-3.9083
C27	-4.2615	-6.9329	-4.5337
C28	-3.392	-8.0297	-4.5189
C29	-2.1549	-7.9339	-3.8922
O30	-2.2424	-4.4564	-2.6959
C31	-2.7586	-3.9977	-1.5543
S32	-4.0203	-4.7703	-0.6989
S33	-2.0796	-2.5542	-0.947
H34	5.8683	-3.3559	1.9272
H35	9.1141	-4.3937	-0.6893
H36	7.8591	-6.4443	-1.414
H37	4.642	-5.3817	1.2177
H38	4.0473	-9.2501	-0.4074
H39	1.7449	-9.4501	-1.3765
H40	1.9705	-5.3693	-2.695
H41	4.2453	-5.1806	-1.7634
H42	6.7279	-1.3685	1.4783
H43	-0.2038	-5.6417	-2.1786
H44	10.4822	-1.3108	1.2217
H45	11.9218	0.6176	1.878
H46	10.8777	2.6682	2.8366
H47	8.4034	2.7736	3.1257
H48	-4.5477	-4.8761	-3.9136
H49	-5.2228	-7.001	-5.0342
H50	-3.6795	-8.9559	-5.0079
H51	-1.46	-8.7669	-3.8832
S52	-3.3311	-1.1691	2.4194
S53	-5.7491	-2.8443	2.1092
C54	-4.9231	-1.5669	2.8865
O55	6.712	0.8457	2.5609
C56	5.8944	1.686	1.9226
S57	4.3042	1.8001	2.5307
S58	6.3525	2.6074	0.5575
S59	2.1402	4.7396	1.3932
S60	3.8473	5.0545	-0.9952
C61	2.5426	5.5941	-0.0292
O62	1.7825	6.6542	-0.3054
C63	2.0075	7.5135	-1.3975
C64	0.9339	7.721	-2.2774
C65	3.2068	8.2117	-1.5049
C66	-0.3554	7.0373	-2.0955
C67	1.1246	8.6464	-3.3199
C68	3.3653	9.1209	-2.5495
H69	3.9962	8.048	-0.7807
N70	-1.3638	7.3273	-2.8326
H71	-0.4142	6.3075	-1.2807
C72	2.3248	9.3322	-3.4609
H73	0.2972	8.8098	-4.002
H74	4.2992	9.6668	-2.6451
C75	-2.5906	6.6672	-2.6559
H76	2.4505	10.0411	-4.274
C77	-3.7592	7.4104	-2.8963

C78	-2.7174	5.3141	-2.2909
C79	-5.0151	6.8467	-2.7058
H80	-3.6578	8.4455	-3.2068
C81	-3.9729	4.7333	-2.1313
H82	-1.8289	4.7011	-2.1696
C83	-5.1232	5.5092	-2.3143
H84	-5.9214	7.422	-2.8657
H85	-4.0614	3.6832	-1.8729
O86	-6.4001	4.9932	-2.2229
C87	-6.7486	4.1122	-1.2204
C88	-7.8153	3.2502	-1.4989
C89	-6.1582	4.1124	0.0475
C90	-8.2788	2.3818	-0.518
H91	-8.273	3.2842	-2.4824
C92	-6.6041	3.2134	1.013
H93	-5.3633	4.8124	0.2804
C94	-7.6569	2.322	0.741
H95	-9.1099	1.7132	-0.7194
H96	-6.1578	3.2316	2.0031
N97	-8.1447	1.3949	1.6791
C98	-7.3121	0.7845	2.4393
C99	-7.7538	-0.1405	3.492
H100	-6.2298	0.9214	2.3342
C101	-9.1039	-0.246	3.8681
C102	-6.8321	-0.9489	4.1746
C103	-9.4976	-1.1113	4.8837
H104	-9.8242	0.3726	3.343
C105	-7.2016	-1.8093	5.2001
O106	-5.4627	-0.8254	3.858
C107	-8.5484	-1.8896	5.5554
H108	-10.5456	-1.1757	5.1616
H109	-6.4437	-2.4024	5.7009
H110	-8.8536	-2.559	6.3541
Cu111	-3.7481	-2.8653	0.7598
Cu112	4.1098	3.4785	0.8162

Table S11. Cartesian coordinates for optimized geometry of **5**.

Atom Type	**Coordinates (Angstroms)**		
	X	**Y**	Z
C1	3.4423	-0.2961	2.585
C2	3.5252	0.9957	2.0399
C3	2.4316	1.8673	2.1848
C4	1.2772	1.4546	2.8449
C5	1.1947	0.1541	3.3453
C6	2.2806	-0.716	3.2317
O7	0.0448	-0.2883	3.9816
C8	-1.0952	-0.4963	3.2303
C9	-1.1314	-0.4174	1.8346
C10	-2.3217	-0.6717	1.1583
C11	-3.4802	-1.0317	1.8545
C12	-3.4378	-1.0967	3.2554
C13	-2.2548	-0.826	3.9399
N14	4.6733	1.3578	1.2879
N15	-4.6563	-1.3395	1.1058
C16	5.1171	2.5902	1.368
C17	-5.2101	-2.5099	1.2963
C18	6.1451	3.2154	0.5983
C19	-6.3339	-3.0794	0.6133
C20	6.4711	4.5579	0.9414
C21	7.4154	5.2792	0.2463
C22	8.0722	4.667	-0.8454
C23	7.7837	3.3702	-1.2161
C24	6.8217	2.5895	-0.5124
C25	-6.9874	-2.4651	-0.5153
C26	-8.0376	-3.195	-1.1394
C27	-8.4312	-4.4345	-0.6758
C28	-7.7953	-5.0348	0.4325
C29	-6.7631	-4.362	1.05
O30	6.5911	1.3735	-0.9054
O31	-6.655	-1.3012	-0.998
C32	-2.4316	1.8664	-2.1853
C33	-3.5253	0.995	-2.0403

C34	-3.4427	-0.2968	-2.5851
C35	-2.281	-0.7171	-3.2316
C36	-1.1949	0.1528	-3.3454
C37	-1.2772	1.4534	-2.8453
O38	-0.0451	-0.29	-3.9815
C39	1.095	-0.4976	-3.2302
C40	1.1311	-0.4185	-1.8345
C41	2.3214	-0.6725	-1.1581
C42	3.48	-1.0324	-1.8542
C43	3.4377	-1.0976	-3.2551
C44	2.2547	-0.8272	-3.9397
N45	-4.6734	1.3574	-1.2883
N46	4.6561	-1.3399	-1.1054
C47	-5.117	2.5899	-1.3686
C48	5.2101	-2.5102	-1.2957
C49	-6.1448	3.2155	-0.5989
C50	6.3339	-3.0795	-0.6126
C51	-6.4705	4.558	-0.9422
C52	-7.4145	5.2796	-0.2471
C53	-8.0715	4.6677	0.8446
C54	-7.7834	3.3709	1.2155
C55	-6.8216	2.5899	0.5118
C56	6.9874	-2.4649	0.5159
C57	8.0377	-3.1946	1.1401
C58	8.4314	-4.434	0.6767
C59	7.7957	-5.0347	-0.4314
C60	6.7633	-4.3622	-1.049
O61	-6.5913	1.3738	0.9049
O62	6.6548	-1.3009	0.9984
H63	4.2927	-0.966	2.4894
H64	2.4647	2.8554	1.7362
H65	0.4259	2.1216	2.9398
H66	2.2022	-1.7177	3.6419
H67	-0.2379	-0.1685	1.2753
H68	-2.3474	-0.6303	0.0741
H69	-4.3396	-1.3414	3.8095
H70	-2.2137	-0.8686	5.0236
H71	4.6502	3.2376	2.1171
H72	-4.7459	-3.1612	2.0447
H73	5.9485	5.0139	1.7803
H74	7.6502	6.3009	0.5274
H75	8.818	5.2279	-1.4037
H76	8.2853	2.8947	-2.0532
H77	-8.5227	-2.7287	-1.9914
H78	-9.2445	-4.9567	-1.1744
H79	-8.1109	-6.011	0.787
H80	-6.2516	-4.8129	1.8984
H81	-2.4645	2.8546	-1.7369
H82	-4.2932	-0.9667	-2.4894
H83	-2.2028	-1.719	-3.6417
H84	-0.4258	2.1202	-2.9403
H85	0.2376	-0.1698	-1.2752
H86	2.3471	-0.6309	-0.0739
H87	4.3395	-1.3422	-3.8092
H88	2.2136	-0.87	-5.0234
H89	-4.65	3.2371	-2.1178
H90	4.746	-3.1618	-2.044
H91	-5.9478	5.0138	-1.7812
H92	-7.6491	6.3014	-0.5283
H93	-8.8171	5.2289	1.4029
H94	-8.285	2.8955	2.0527
H95	8.5228	-2.728	1.992
H96	9.2448	-4.956	1.1754
H97	8.1113	-6.0109	-0.7858
H98	6.2519	-4.8133	-1.8974
Co99	5.629	0.0259	0.0615
Co100	-5.6291	0.0259	-0.0615

Table S12. Cartesian coordinates for optimized geometry of **7**.

Atom Type	**Coordinates (Angstroms)**		
	X	**Y**	Z
C1	-3.5249	0.1404	-2.347

C2	-3.4959	1.0953	-1.3193
C3	-2.2642	1.6603	-0.9522
C4	-1.0909	1.29	-1.6036
C5	-1.1362	0.3408	-2.6278
C6	-2.3531	-0.2331	-3.0022
O7	-7E-4	-0.0106	-3.3374
C8	1.1364	-0.3565	-2.6277
N9	-4.7088	1.4547	-0.6712
C10	2.3511	0.2218	-3.0023
C11	3.5242	-0.147	-2.3467
C12	3.4987	-1.1015	-1.3186
C13	2.2691	-1.671	-0.9513
C14	1.0946	-1.3055	-1.603
N15	4.7129	-1.4561	-0.6704
C16	-4.959	2.7272	-0.486
C17	4.968	-2.7276	-0.4849
C18	-6.0926	3.32	0.1419
C19	6.1039	-3.316	0.143
C20	-6.1358	4.7411	0.1952
C21	-7.1996	5.415	0.7505
C22	-8.2831	4.668	1.2698
C23	-8.2882	3.2905	1.228
C24	-7.1937	2.5564	0.6768
C25	7.2023	-2.5482	0.6774
C26	8.2996	-3.2781	1.2286
C27	8.2995	-4.6556	1.2708
C28	7.2187	-5.4067	0.752
C29	6.1523	-4.7369	0.1967
O30	-7.2412	1.2656	0.687
O31	7.2451	-1.2572	0.6873
C32	2.264	1.6631	0.952
C33	3.4954	1.097	1.3187
C34	3.5239	0.1421	2.3463
C35	2.352	-0.2306	3.0019
C36	1.1355	0.3443	2.6278
C37	1.0907	1.2937	1.6037
O38	-2E-4	-0.0061	3.3376
C39	-1.1372	-0.3531	2.6281
N40	4.7084	1.4556	0.6704
C41	-2.3522	0.2243	3.0028
C42	-3.5252	-0.1455	2.3475
C43	-3.499	-1.1	1.3194
C44	-2.2691	-1.6686	0.952
C45	-1.0947	-1.3021	1.6035
N46	-4.7131	-1.4555	0.6713
C47	4.9594	2.7279	0.485
C48	-4.9673	-2.7271	0.4859
C49	6.0931	3.3201	-0.1433
C50	-6.1028	-3.3163	-0.142
C51	6.1372	4.7411	-0.1967
C52	7.2012	5.4143	-0.7525
C53	8.2839	4.6665	-1.2723
C54	8.2882	3.289	-1.2305
C55	7.1935	2.5557	-0.6786
C56	-7.202	-2.5492	-0.6758
C57	-8.2989	-3.2797	-1.227
C58	-8.2978	-4.6572	-1.2695
C59	-7.2163	-5.4077	-0.7512
C60	-6.1502	-4.7372	-0.196
O61	7.2402	1.2648	-0.6888
O62	-7.2458	-1.2582	-0.6854
H63	-4.4759	-0.2959	-2.6392
H64	-2.2264	2.3753	-0.1355
H65	-0.1388	1.7237	-1.3168
H66	-2.3697	-0.9607	-3.8074
H67	2.365	0.949	-3.8078
H68	4.4736	0.2926	-2.639
H69	2.2338	-2.3857	-0.1342
H70	0.144	-1.7427	-1.3165
H71	-4.2271	3.4374	-0.8848
H72	4.2387	-3.4408	-0.8833
H73	-5.2965	5.2964	-0.2198
H74	-7.2132	6.4998	0.7837

H75	-9.1313	5.1906	1.706
H76	-9.1184	2.7126	1.6218
H77	9.1278	-2.6971	1.6221
H78	9.1498	-5.175	1.707
H79	7.2363	-6.4915	0.7855
H80	5.3149	-5.2954	-0.2179
H81	2.2265	2.3782	0.1354
H82	4.4746	-0.2949	2.6383
H83	2.3682	-0.9582	3.807
H84	0.1387	1.7282	1.3174
H85	-2.3666	0.9515	3.8083
H86	-4.4749	0.2935	2.6399
H87	-2.2334	-2.3832	0.1349
H88	-0.1438	-1.7385	1.3167
H89	4.228	3.4387	0.8838
H90	-4.2374	-3.4398	0.8841
H91	5.2984	5.2969	0.2187
H92	7.2155	6.499	-0.7858
H93	9.1322	5.1886	-1.709
H94	9.1178	2.7106	-1.6247
H95	-9.1275	-2.6992	-1.6201
H96	-9.1477	-5.1771	-1.7056
H97	-7.2331	-6.4924	-0.7849
H98	-5.3123	-5.2952	0.2184
Cu99	-5.9552	0.0016	4E-4
Cu100	5.9544	0.0017	1E-4

Anticancer Activity

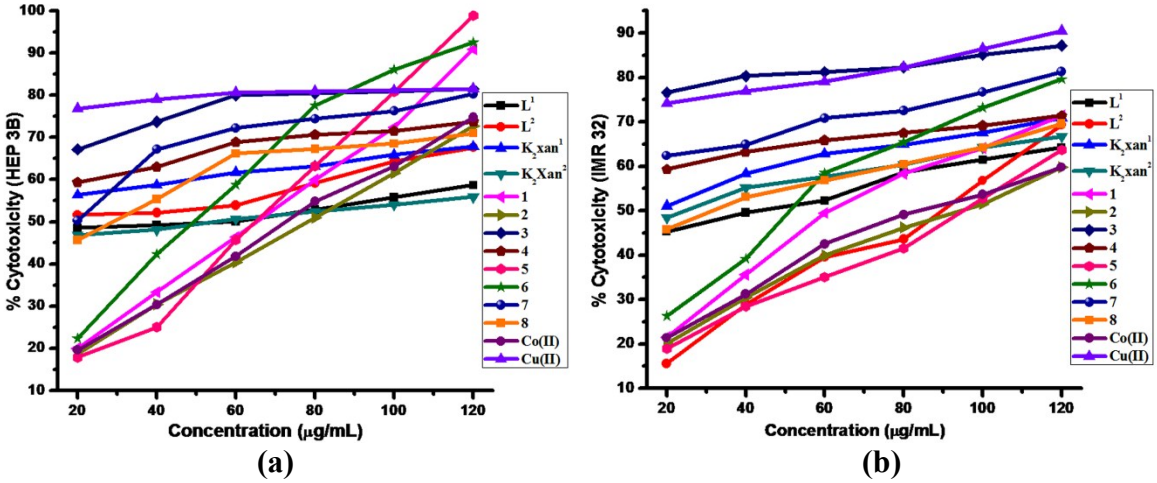

(a) **(b)**

Figure S29. % Cytotoxicity observed for investigated compounds against HEP 3B (a) and IMR 32 (b) at different concentrations.

In analogy to the literature reports on antitumour activity of similar compounds, our hypothesis on binuclear Co^{II}/Cu^{II} xanthate complexes induce cytotoxicity might involve multiple mode of action leading to the cell death, can be explained by several previously observed effects of isostructural dithiocarbamate complexes and complexes derived from *N, O*- donor ligands. 1,1-dithio moieties are known to exert cytotoxicity through antiangio-genesis effects, inhibition of numerous metalloenzymes and NF-KB-related gene-expression and modulation of cellular

metabolism, which lead to tissue damage.[14] The decomposition and metabolic products of a transition metal 1,1-dithio complexes in vivo, *ca* free 1,1-dithio moieties, CS_2 are reportedly able to arrest the cell proliferation.[15] Dou and co-workers reported several studies concerning the cytotoxic activity of discrete, transition metal complexes, including complexes based on *S*, *N* and/ or *O*- donor ligands.[16] Electrochemical and stability data[17] suggests that the most stable dithiocarbamate complexes proved to be most cytotoxic in vitro and also against the cisplatin-resistant. Recent investigations highlights the electronic density analysis of different dithiocarbamate metal complexes to correlate their toxicity as well as the ability to inhibit proteasome and induce apoptosis in human cancer cells.[18] It has appeared that the dithiocarbamate complexes holding higher electronic density over sulfur atom within the complex are more active against the JAMM domain of the 26S proteasome.[18] Due to presence of almost similar structural and electronic features in dithiocarbamate and xanthate complexes, analogous mode of action for the antitumor activity could be expected for both of them.Beyond this, the possibility of transchelation reactions with physiological molecules and metabolic products of xanthate complexes could alter the intracellular metal constitutions which lead to the cytotoxic activity. Further, cobalt and copper complexes are also known to target DNA under physiological conditions via an oxidative pathway[19] and induce cytotoxicity.[20]

Moreover, several stereoelectronic parameter made available by DFT study are known to provide insight in the mechanisms related to membranes transportations, revealing possible interactions with biological macromolecules or intracellular receptors and thus provide a possible rationalization for the structure activity relationships (SARs) of these compounds. The stability and reactivity of the molecules towards possible biological receptors such as electron rich or electron deficient regions are reportedly depends on the frontier orbitals,[21] as HOMO energy is closely related to susceptibility to electrophilic attack while LUMO energy is closely related to susceptibility to nucleophilic attack.

Table S13. Parameters obtained from the computational investigations and cytotoxic activity for model compounds.

Compound	E_{HOMO} (eV)	HOMO-LUMO gap (eV)	Dipole moment (Debye)	Charges on chelated atoms (S/N,O) and metal center	IC_{50} values	
					HEP 3B µM (1mL) ±SE	IMR 32 µM (1mL) ±SE
L_1	-5.59	3.7829	3.4765	N,O – (0.568-0.600)	137.8±13.9	104.0±3.3
Kxan-1	-5.0127	3.2543	17.2480	S –(0.380-0.394), K (0.821-0.824)	17.8±2.9	23.2±1.4
1	-5.5524	3.4646	2.6945	S – (0.020-0.036), Co (0.052)	52.9±1.3	51.8±2.9
3	-5.5772	3.3941	1.1886	S (0.015-0.028), Cu –(0.103-0.109)	8.1±0.8	1.9±0.3
5	-5.4240	3.5688	0.4366	N – (0.566-0.571), O – (0.654- 0.661), Co (0.749-0.750)	69.7±3.6	99.7±6.6
7	-5.4801	3.6303	0.0139	N – (0.545), O – (0.606), Cu (0.607)	19.2±2.1	13.2±1.1

Induction of Apoptosis study

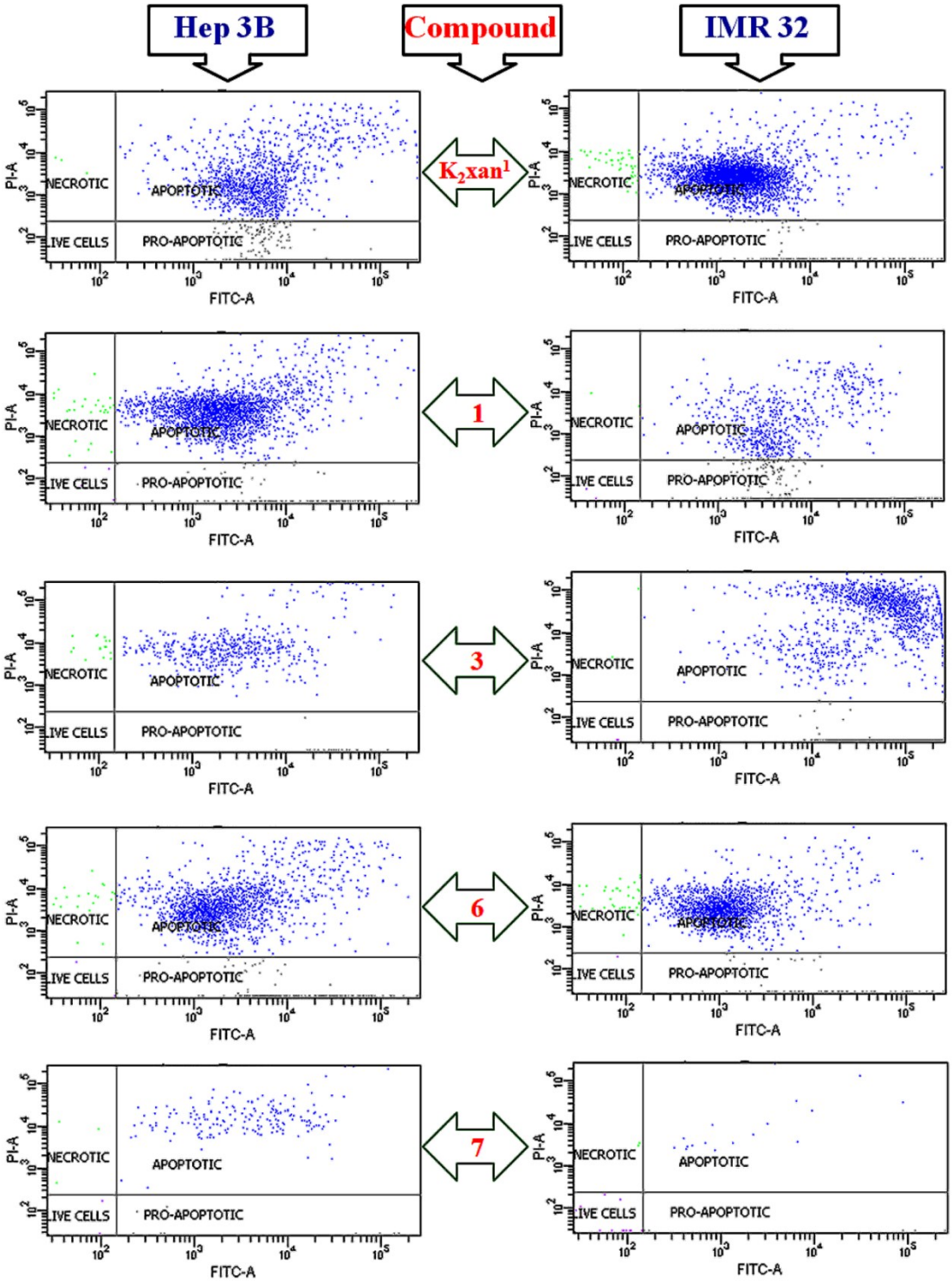

Figure S30: Flow cytometry density plots of HEP 3B and IMR 32 upon treatment with **K_2xan[1]**, binuclear macrocyclic complexes **1**, **3**, **6** and **7**.

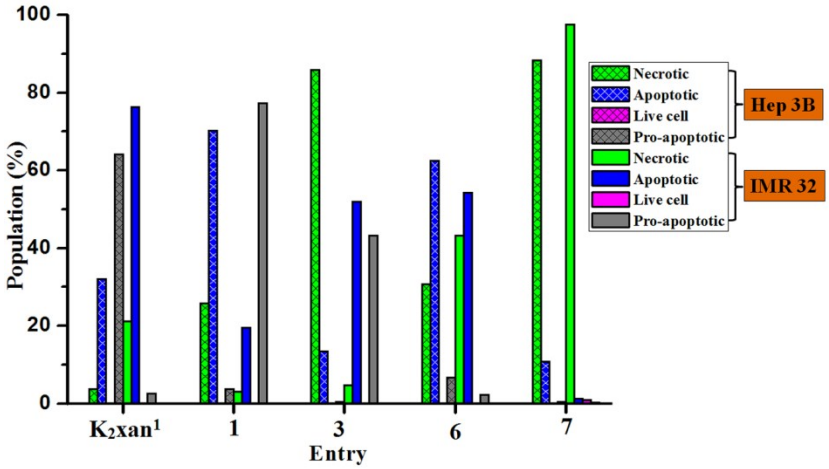

Figure S31. Flow cytometry data revealing apoptotic/ necrotic/live cell population of HEP 3B and IMR 32 cells upon treatment of **K_2xan^1**, binuclear macrocyclic complexes **1**, **3**, **6** and **7**.

Thermogravimetric Analysis

The thermogravimetric analysis of bimetallic xanthate/ *N,O*-Schiff base macrocyclic complexes **1-8,** were performed under N_2 atmosphere at a heating rate of 10 °C /min from room temperature to 550 °C. The thermal analysis data and corresponding thermogram are summarized in Table S12 and Figure S31, respectively. A single or multi stage mass loss for these compounds was observed with DTG and corresponding DTA curves which are ascribed to endothermic and/or exothermic elimination of molecular fragments due to the thermal degradation. The bimetallic xanthate macrocyclic complexes **1-4**, exhibit an insignificant mass loss of ~ 1% in initial stage which could be assigned to the loss of solvent impurities. Further mass loss of 12.44, 8.07, 4.2 and 3.52 % observed in the second stage of degradation is attributed to the loss of CS_2/ SCO ligand fragments. The maximum rate of decomposition seen on DTG curves for **1-4** is 360.2, 442.3, 327.8 and 337.6 °C respectively. Contrarily, among bimetallic *N,O*-Schiff base complex **5-8**, complex **5** display an endothermic peak at 147.2 °C on DTA curve without mass loss suggesting phase changes occurring due to its melting. Further it exhibits a single stage degradation started at 200 °C and continues at 550 °C with maximum rate of decomposition observed at 269.8 °C on DTG curve. Other complexes **6-8** showed two stages of degradation involving the loss of naphthyl/ CH_2Cl_2 fragments in the first stage followed by a continuous mass loss with a maximum rate of degradation at 467.5, 373.9 and 358.3 °C observed on corresponding DTG curves. It may be noted that the thermogravimetric study of complex **7** has been performed with the crystals obtained from CH_2Cl_2/hexane solvent mixture. The association of two CH_2Cl_2 molecules with the crystals is indeed confirmed by its thermogram, disclosing a mass loss of 14.8% at 212 °C corresponding to $2CH_2Cl_2$ molecules (calc. 16.5%). This is consistent with the results of single crystal X-ray analysis of **7**.

Table S14. Thermogravimetric analysis of binuclear xanthate/ *N,O*-Schiff base macrocyclic complexes **1-8.**

Entry	DTA (°C) (μV)	DTG (°C) (μg/min)	Significant Mass loss % (temp range °C)	Inference
1	188.5 (8.21)	188.1 (45.2) 360.2 (20.3)	1.22 % (upto 100) 12.44 % (100-250) 22.71 % (250-550) 36.37 % (50-550)	1st stage: Insignificant mass loss of solvent impurities. 2nd stage: Loss of $2CS_2$ molecules (calc. 12.3 %). 3rd stage: Decomposition continues after 550 °C. - Maximum rate of decomposition observed at 188.1 °C on DTG curve.
2	…	442.3 (62.2)	1.49 % (upto 100) 8.07 % (100-350) 23.43 % (350-550) 32.99 % (100-550)	1st stage: Insignificant mass loss of solvent impurities. 2nd stage: Loss of 2SCO fragment (calc. 8.35 %). 3rd stage: Decomposition continues after 550 °C. - Maximum rate of decomposition observed at 442.3 °C on

				DTG curve.
3	205.2 (2.57) 298.7 (2.42)	327.8 (145.4)	0.5 % (upto 100) 4.2 % (100-250) 25.4 % (250-550) 30.1 % (50-550)	1st stage: Insignificant mass loss of solvent impurities. 2nd stage: Loss of SCO fragment (calc. 4.8 %). 3rd stage: Decomposition continues after 550 °C. - Maximum rate of decomposition observed at 327.8 °C on DTG curve.
4	264.2 (3.32) 303.5 (4.46) 329.8 (2.84) 362.8 (-1.66)	337.6 (154.0) 353.4 (132.4)	3.52 % (50-100) 35.68 % (100-550) 39.20 %(50-550)	1st stage: Loss of SCO (calc. 4.1 %). 2nd stage: Decomposition continues after 550 °C. - Maximum rate of decomposition observed at 337.6 °C on DTG curve.
5	**147.2 (25.8)**	269.8 (104.7)	47.8 % (200-550)	1st stage: Decomposition continues after 550 °C. - *An endothermic peak at 147.2 °C appeared on DTA curve without mass loss suggesting phase changes occurring due to its melting.* - Maximum rate of decomposition observed at 269.8 °C on DTG curve.
6	**…**	77.3 (31.8) 459.2 (153.9) 467.5 (158.5)	10.6 % (upto 300) 39.8 % (300-550) 50.4 % (50-550)	1st stage: Loss of naphthyl (calc. 11.23 %). 2nd stage: Decomposition continues after 550 °C. - Maximum rate of decomposition observed at 467.5 °C on DTG curve.
7	212.1 (7.75) 349.1 (6.50)	212.1 (131.6) 373.9 (150.2)	14.8 % (150-250) 35.2 % (250-550) 50.0 % (50-550)	1st stage: Loss of $2CH_2Cl_2$ (calc. 14.8 %). 2nd stage: Decomposition continues after 550 °C. - Maximum rate of decomposition observed at 373.9 °C on DTG curve.
8	364.6 (39.59)	358.3 (93.1)	12.2 % (50-250) 48.5 % (250-550) 60.7% (100-550)	1st stage: Loss of naphthyl (calc. 16.5%). 2nd stage: Decomposition continues after 550 °C. - Maximum rate of decomposition observed at 358.3 °C on DTG curve.

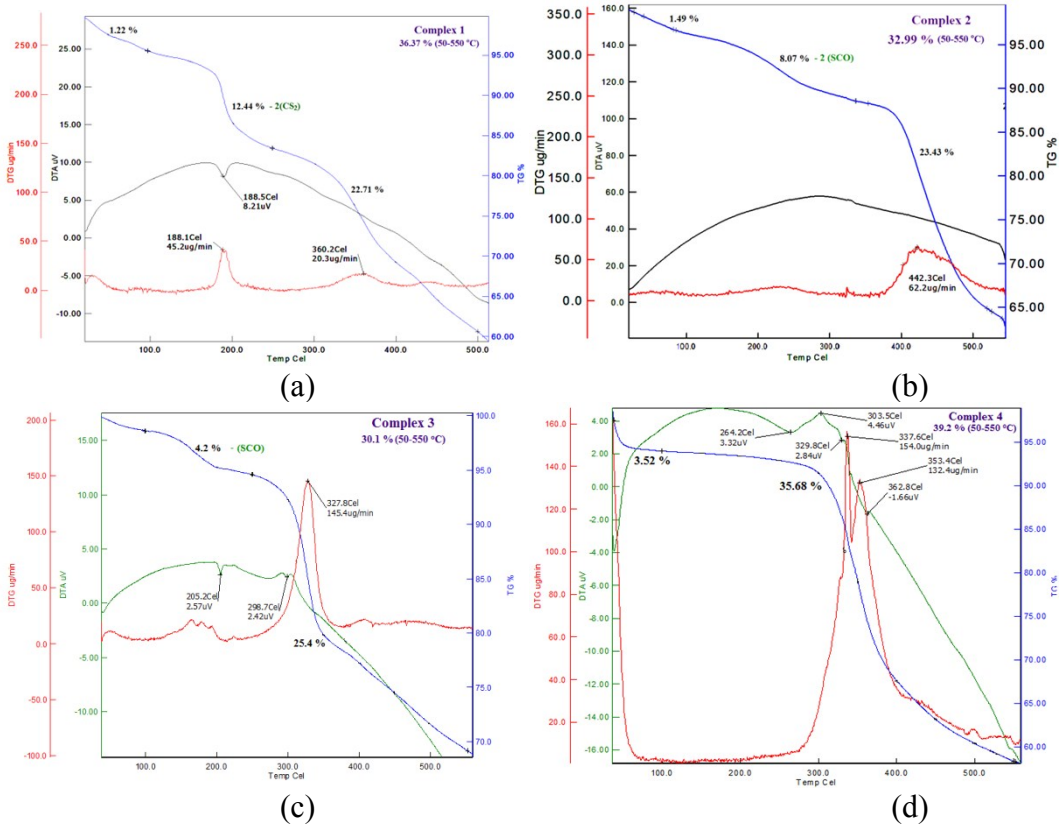

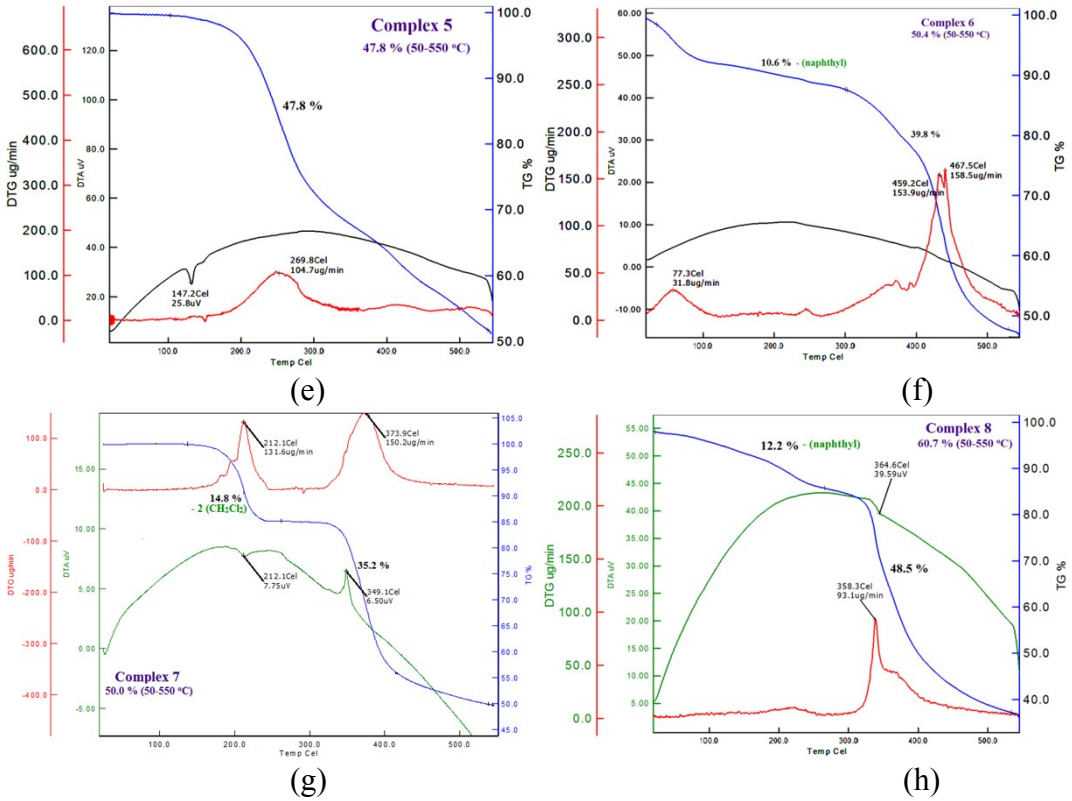

Figure S32. DTG/DTA/TG curves a-h for binuclear xanthate/ *N,O*-Schiff base macrocyclic complexes 1-8, respectively.

References:

1. (a) M. Thirumavalavan, P. Akilan, M. Kandaswamy, *Inorg. Chem***. 2003**, *42*, 3308. (b) A. S. A. Zidan, *Synth React Inorg Met. Org. chem*. **2001**, *31*, 457.
2. (a) H. P. S. Chauhan, A. Bakshi, *J Therm. Anal. Calorim.*, **2011**, 105, 937. (b) A.; Singhal, D. P. Dutta, A. K. Tyagi, M. M. Shaikh, P. Mathur, I. Lieberwirth, *J. Organomet. Chem.*, **2007**, 692, 5285.
3. 'POWDERX'' – A program for indexing and refinement of X-ray data written by Dr. V. K. Wadhavan, Bhabha Atomic research Center, private communication.
4. S. K. Verma, R. Kadu, V. K. Singh, *Synth. React. Inorg., Met.-Org., Nano-Met. Chem*. **2014**, *44*, 441.
5. L.-Q. Chai, G. Wang, Y.-X. Sun, W.-K. Dong, L. Zhao, X.-H. Gao, *J. Coord. Chem*. **2012**, *65*, 1621.
6. R. Pandey, P. Kumar, A. K. Singh, M. Shahid, P. Z. Li, S. K. Singh, Q. Xu, A. Misra, D. S. Pandey, *Inorg. Chem*. **2011**, *50*, 3189.
7. S. Sreedaran, K. S. Bharathi, A. K. Rahiman, L. Jagadish, V. Kaviyarasan, V. Narayanan, *Polyhedron* **2008**, *27*, 2931.
8. M. J. Frisch, G. W. Trucks, H. B. Schlegel, G. E. Scuseria, M. A. Robb, J. R. Cheeseman, J. A. Montgomery Jr., T. Vreven, K. N. Kudin, J. C. Burant, J. M. Millam, S. S. Iyengar, J. Tomasi, V. Barone, B. Mennucci, M. Cossi, G. Scalmani, N. Rega, G. A. Petersson, H. Nakatsuji, M. Hada, M. Ehara, K. Toyota, R. Fukuda, J. Hasegawa, M. Ishida, T. Nakajima, Y. Honda, O. Kitao, H. Nakai, M. Klene, X. Li, J. E. Knox, H. P. Hratchian, J. B. Cross, C. Adamo, J. Jaramillo, R. Gomperts, R. E. Stratmann, O. Yazyev, A. J. Austin, R. Cammi, C. Pomelli, J. W. Ochterski, P. Y. Ayala, K. Morokuma, G. A. Voth, P.

Salvador, J. J. Dannenberg, V. G. Zakrzewski, S. Dapprich, A. D. Daniels, M. C. Strain, O. Farkas, D. K. Malick, A. D. Rabuck, K. Raghavachari, J. B. Foresman, J. V. Ortiz, Q. Cui, A. G. Baboul, S. Clifford, J. Cioslowski, B. B. Stefanov, G. Liu, A. Liashenko, P. Piskorz, I. Komaromi, R. L. Martin, D. J. Fox, T. Keith, M. A. A.-Laham, C. Y. Peng, A. Nanayakkara, M. Challacombe, P. M. W. Gill, B. Johnson, W. Chen, M. W. Wong, C. Gonzalez, J. A. Pople, Gaussian, Inc., Wallingford, CT, 2004.

9. S. Salehzadeh, M. Bayat, *Comp. Theor.Chem*. **2011**, *965*, 131.
10. K. G. Vladimirova, A. Y. Freidzon, O. V. Kotova, A. A. Vaschenko, L. S. Lepnev, A. A. Bagatur'yants, A. G. Vitukhnovskiy, N. F. Stepanov, M. V. Alfimov, *Inorg. Chem*. **2009**, *48*, 11123.
11. (a) V. K. Singh, R. Kadu, H. Roy, *Eur. J. Med. Chem.* **2014**, *74*, 552. (b) R. Kadu, V. K. Singh, S. K. Verma, P. Raghavaiah, M. M. Shaikh *J Mol. Struct*. **2013**, *1033*, 298.
12. (a) S. R. Gadre, P. K. Bhadane*, Resonance*, **1999**, *4*, 11. (b) F. A. Bulat, A. T.-Labbé, T. Brinck, J. S. Murray, P. Politzer, *J Mol Model* **2010**, *16*, 1679. (c) P. Politzer, P. R. Laurence, K. Jayasuriya, *Environ. Health Perspect.* **1985**, *61*, 191.
13. S. R. Peerannawar, S. P. Gejji *Phys. Chem. Chem. Phys*., **2012**, ***14***, 8711.
14. (a) S. P. Bach, R. Chinery, S. T. O'Dwyer, C. S. Potten, R. J. Coffey, A. J. Watson, *Gastroenterology* **2000**, *118*, 81. (b) K. G. Daniel, D. Chen, S. Orlu, Q. C. Cui, F. R. Miller, Q. P. Dou, *Breast Cancer Res.* **2005**, *7*, R897. (c) N. Segovia, G. Crovetto, P. Lardelli, M. Espigares, *J. Appl. Toxicol*. **2002**, *22*, 353. (d) O. M. Viquez, H. L. Valentine, K. Amarnath, D. Milatovic, W. M. Valentine, *Toxicol. Appl. Pharmacol*. **2008**, *229*, 77. (e) M. Chabicovsky, E. P.-Grassauer, J. Seipelt, T. Muster, O. H. J. Szolar, A. Hebar, O. D.-Dier, *Basic Clin. Pharmacol. Toxicol.* **2010**, *107*, 758. (f) E. M. Nagy, S. Sitran, M. Montopoli, M. Favaro, L. Marchiò, L. Caparrotta, D. Fregona, *J Inorg. Biochem*. **2012**, *117*, 131. (g) Y. Qian, G.-Y. Ma, Y. Yang, K. Cheng, Q.-Z. Zheng, W.-J. Mao, L. Shi, J. Zhao, H.-L. Zhu, *Bioorg. Med. Chem*. **2010**, *18*, 4310.
15. (a) V. Amarnath, K. Amarnath, W. M. Valentine, *Curr. Top. Toxicol.* **2007**, *4*, 39. (b) J. I. Garcia, E. Humeres, *J. Org. Chem.* **2002**, *67*, 2755. (c) E. Humeres, N. A. Debacher, J. D. Franco, B. S. Lee, A. Martendal, *J. Org. Chem.* **2002**, *67*, 3662.
16. (a) V. Milacic, D. Chen, L. Ronconi, K. R. L.-Piwowar, D. Fregona, Q. P. Dou, *Cancer Res.* **2006**, *66*, 10478. (b) D. Chen, Q. Z. C. Cui, H. J. Yang, Q. P. Dou, *Cancer Res.* **2006**, *66*, 10425. (c) K. G. Daniel, P. Gupta, R. H. Harbach, W. C. Guida, Q. P. Dou, *Biochem. Pharmacol.* **2004**, *67*, 1139. (d) D. Chen, M. Frezza, R. Shakya, Q. C. Cui, V. Milacic, C. N. Verani, Q. P. Dou, *Cancer Res.* **2007**, *67*, 9258. (e) D. Chen, F. Peng, Q. C. Cui, K. G. Daniel, S. Orlu, J. Liu, Q. P. Dou, *Front. Biosci*. **2005**, *10*, 2932**.**
17. F. K. Keter, I. A. Guzei, M. Nell, W. E. van Zyl, J. Darkwa, *Inorg. Chem*. **2014**, *53*, 2058.
18. (a) B. Cvek, V. Milacic, J. Taraba, Q. P. Dou, *J. Med. Chem*. **2008**, *51*, 6256. (b) V. Milacic, D. Chen, L. Giovagnini, A. Diez, D. Fregona, Q. P. Dou, *Toxicol. Appl. Pharmacol.* **2008**, *231*, 24.
19. (a) R. Buchtik, Z. Travnicek, J. Vanco, R. Herchel, Z. Dvorak, *Dalton Trans*. **2011**, *40*, 9404. (b) S. S. Bhat, A. A. Kumbhar, H. Heptullah, A. A. Khan, V. V. Gobre, S. P. Gejji, V. G. Puranik, *Inorg. Chem*. **2011**, *50*, 545.
20. L. F. Chin, S. M. Kong, H. L. Seng, K. S. Khoo, R. Vikneswaran, S. G. Teoh, M. Ahmad, S. B. A. Khoo, M. J. Maah, C. H. Ng, *J. Inorg. Biochem*. **2011**, *105*, 339.
21. G. L. Parrilha, J. G. da Silva, L. F. Gouveia, A. K. Gasparoto, R. P. Dias, W. R. Rocha, D. A. Santos, N. L. Speziali, H. Beraldo, *Eur. J. Med. Chem*. **2011**, *46*, 1473.